

## Schedule for Presentation Meeting of Master-Degree Thesis in 2021

### International Program of Maritime & Urban Engineering

Date : July 28th (Wednesday) starting from 09:30

Venue : S1- 312 Lecture Room

**15 min. Oral presentation + 10 min. Q&A session**

| No.         | Time        | Name                         | Supervisor | Title of thesis   | Chairperson |
|-------------|-------------|------------------------------|------------|---|-------------|
| 1           | 9:30-9:55   | ALSHERFAWI ALJAZAERLY Alaa   | Kita       | Urban morphological changes in the late modern era of Damascus city   | Araki       |
| 2           | 9:55-10:20  | HUANG Ruoyi                  | Irie       | Impacts of Yangtze river water transfer on water quality in Lake Taihu, China   |             |
| 3           | 10:20-10:45 | SHI Kanbei                   | Doi        | Investigating users' acceptance on battery-swapping electric two-wheelers   |             |
| 4           | 10:50-11:15 | HUANG Wenjia                 | Ma         | Residual stress in wire and arc additive manufacturing using low transformation temperature material 10Cr-10Ni                      | Inui        |
| 5           | 11:15-11:40 | FUNDORA CAMPOS Sila Mercedes | Aoki       | Effect of horizontal plates on the sliding of breakwater caissons   |             |
| Lunch break |             |                              |            |   |             |
| 6           | 13:00-13:25 | CHAN Siyu                    | Suzuki     | Numerical study on derivation of hydrodynamic coefficients of AUV using CFD based on N-S equation of non-inertial coordinate system | Inui        |
| 7           | 13:25-13:50 | LI Junjian                   | Suzuki     | Development of automatic evaluation system of underwater vehicle's motion performance based on OpenFOAM                             |             |
| 8           | 13:50-14:15 | LANGILANGI Colin Fatuimoana  | Maki       | Capsizing & survivability of ships based on safe basin's fractals   | Irie        |
| 9           | 14:20-14:45 | LIN ShenChi                  | Toda       | Microcomputer control of underwater vehicle with undulating side fins   |             |
| 10          | 14:45-15:10 | CHENG Yuxuan                 | Hirohata   | An investigation on patch welding repair for thickness reduction of steel structural compressive member                             |             |

**Meeting for Evaluation:** From 15:30 at S1-312 Lecture Room

Members are Steering committee members and the supervisors

# Urban morphological changes in the late modern era of Damascus City

Alaa Alsherfawi Aljazaerly

Lab 03. Architectural and Urban Planning. Department of Architectural Engineering

**Key Words:** *Damascus, street system, Space Syntax, urban morphology*

## 1. Introduction

Damascus, the capital of Syria, is among the oldest continuously inhabited cities in the world. The long uninterrupted history of Damascus dates back to 3000 BCE (UNESCO, 2009). Through its long history, the city has been under different rulership and has hosted multiple civilizations, from Aramaic through Greeks, Romans, Islamic and finally Ottoman rule. It was later colonized by the French until independence in 1946, when it became the capital city of the Syrian Arab Republic (Burns, 2019; Lababedi, 2008).

Since the early modern era—the end of the Ottoman empire in Syria—Damascus has undergone different socio-spatial, political, and economic changes. These multiple transformations, coupled with rapid urbanization and urban expansion is exerting a significant impact on the urban fabric, especially in the physical configuration of space or urban morphological aspects. In order to comprehend these morphological changes and associated patterns since the late modern era this research aims to answer the following questions:

- What is the spatial configuration of Damascus city urban core between the French mandate and before the civil war?
- What is the logic behind the street pattern of the spatial configuration?
- What are differences between the street morphologies on the local level before the war?

## 2. Methodology

The study employed space syntax methodological tool to analyze the morphological transformation of the Damascus (1929-2004). The timelines were according to major changes such as economic, cultural, and political changes. However, 2004 was set as the reference point to analyze the situation of the city on a local scale. At the local scale, the city is analyzed according to street relational analysis. Based on the time of development and land use, eight cases were chosen for the microanalysis. By comparing the eight cases with the results of the syntactic analysis, it was possible to understand how different morphologies are associated with the different syntactic performances.

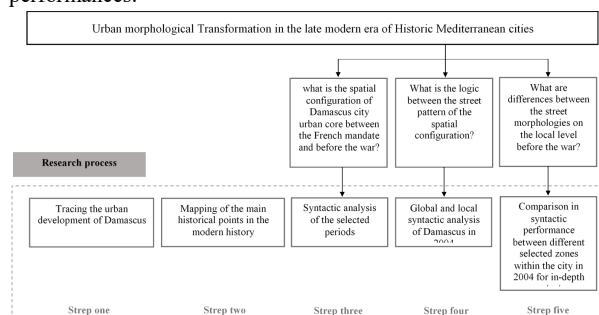


Figure 1: Research Framework

## 3. Findings

### The morphological transformation of Damascus City

According to the results, the city kept its traditional morphology during the early years of the French mandate (1929). The organic streets and hierarchy are visible on the axial map as there is variance in the length of the axial lines. The syntactic core followed the shopping streets and commercial zones. As the city was organically expanding, the strong integrated streets segments correspond to the highly populated segments such as the "Haj" route, which had great spatial and also social and economic relevance in the Ottoman era (Al Rahhal, 2015).

However, a new pattern of wide and straight (boulevards) emerged after the first master plan directed by the French, creating a dual street morphology. This master plan was the first city-scale development plan for Damascus. It introduced a foreign pattern to the street structure as the streets became primarily for vehicles rather than pedestrians. The city started to grow towards the north. Consequently, syntactic core shifted towards the north and to the new city commercial center. The city's historic center, which kept its traditional structure, consequently lost its position as strong integration core.

With the second master plan, which had concentrated on zoning the city and link it with the surrounding suburbs, coupled with population increase, new neighborhoods emerged in the city towards the west and south. These new parts had different morphological patterns than the French developed areas and neighborhoods. As the city grew southwards, the integration core extended towards the north-south axis. By 2004 the density of the city had increased, and informal settlements have grown to create a belt around the city. Hence, the integration core expanded in the radial direction with a center between the traditional and new commercial areas.

### Relationship between the parts and whole

The degree of consistency between the local and city-wide analysis reflects how much the city is intelligible (Figure 2 and 3). The areas with high local and city-wide integration values are the most visited parts known as the integration core, reflecting the importance and performance of this area both locally and city scale-wise. In contrast, areas with low values are segregated and gets less activity from the population as a whole. The commercial area in Damascus is located in the geometric and integration center of the city, which probably reflects socio-economic activity in this part of the city.

Informal settlements located at the edge have less connection with the city core. However, some informal settlements, despite having a weak link with the city core, have a very strong local core due to high street connectivity. This situation can be leveraged to potentially reduce the pressure on the integration core through the creation of multiple central poles and thus decentralize the concentration from the city center towards the south.

### Local scale morphologies

The inner system of the areas has strong effect on the local integration values. The results showed that different street morphologies produced different patterns of syntactic performance. The informal settlement which had uniformed street system gave high integration value. However, this high local integration with lack of connection to the city core may not be beneficial on the activity level. Since all street have the same high value then relatively they have low activity as it will be equally distributed on all the streets. Furthermore, the lack of accessibility hierarchy can be translated as lack of privacy hierarchy. Whereas the traditional systems showed less integration values, there is hierarchy in street morphological and syntactic system meaning there is different scales from public to private. The hierarchy gives underlying system to the distribution of function where integrated areas used as commercial and shopping streets and the less integrated as housings.

Commercial areas on the other hand had the highest city-wide integration meaning that these areas are accessible and have high activity degree on the scale of the whole city.

### 4. Conclusion and planning implication

Based on the findings from this study, the following three implications for urban planning and policy are proffered:

- City planners and urban policy makers need to maintain the street pattern of the historic centers to keep its present character of balance between use and activity since it favors a pedestrian environment
- Although the shift in core zones of street activity to the south is necessary to reduce overconcentration, it needs to be managed through integrated metropolitan planning that prioritize connectivity between different areas to prevent segregation of neighborhoods such as informal settlements
- While southern area shows high integration, this is due to the arterial roads or planning street systems for cars. It is important for promote balance in street systems that improve connectivity at city scale and the local scale especially in relation to the pedestrian or human environment.
- There should be the integration on informal neighborhoods that show high integration but segregated from the larger cities. They are potential news cores but need better connectivity to the main city to avoid segregation within the urban realm.
- Pos-war redevelopment should pay attention to the potential of the street patterns in both historic and informal areas to encourage a more people-centered street design that promotes human interaction, movement and diversity in the use of streets.

Overall, through space syntax-based analysis as showed varieties in syntactic performance over different historical periods and over local urban systems. Specifically, the study has demonstrated a dual morphology of street pattern manifested in organic street patterns concentrated in traditional and informal areas, on one hand and preplanned streets in formally planned neighborhoods.

### 5. Future Studies

The major component of space syntax analysis is to undertake empirical or field-based analysis integrate the human behavior and the social dimension of street patterns. Due to the inherent limitation of this study's inability to engage in field analysis,

future studies should employ human behavior analysis. More, there is the need to reference updated and recent maps after 2011 to comprehend the situation after the war.

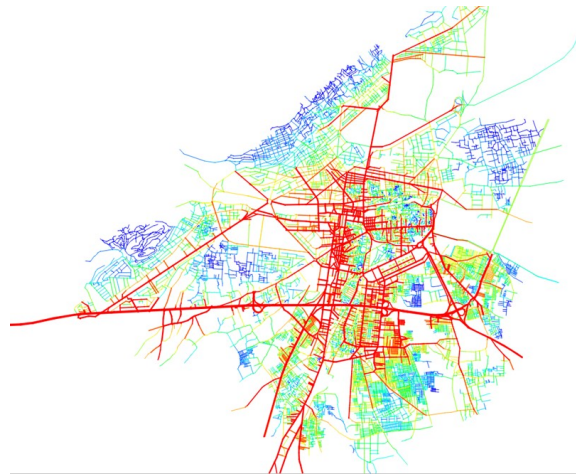


Figure (2): Global integration analysis of Damascus 2004 radii Rn

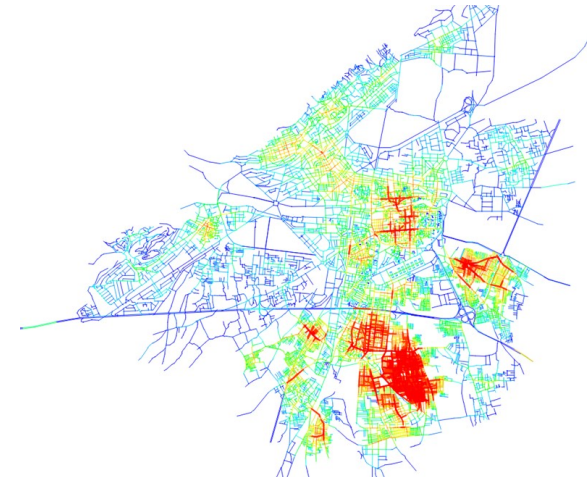


Figure (3): local integration analysis of Damascus 2004 radii 500

### References

- 1) UNESCO (2009) Ancient City of Damascus <https://whc.unesco.org/en/list/20/Hasemura> (retrieved on 20-1-2021)
- 2) Burns, R. (2019). Damascus: A history (Second edition). Routledge.
- 3) Lababedi, Z. (2008). The urban development of Damascus: A study of its past, present and future Masters, (University College London) <https://discovery.ucl.ac.uk/id/eprint/14328/> (retrieved on 01-02-2020)
- 4) Al Rahhal, A. (2015). The Pilgrimage Route and its Service Buildings in Syria during the Ottoman Period (Historical and comparative study). Damascus University

# Impacts of Yangtze River Water Transfer on Water Quality in Lake Taihu, China

Huang Ruoyi

Water Engineering Laboratory, Division of Global Architecture

**Key Words:** Lake Taihu, numerical simulation, water diversion, water quality, SCHISM

## 1. Introduction

The rapid and extensive economic development of China in recent decades has caused eutrophication of lakes. The water quality deterioration of a lake not only affects the ecosystem of the lake itself, but also the lives of local residents and the development of local economy. Therefore, improving the water quality and ecological functions have become urgent tasks.<sup>1)</sup>

The Chinese government has carried out comprehensive treatment of Lake Taihu near Shanghai. The main measures include controlling external pollution, implementing ecological dredging, and scientific water diversion. Water diverted from the Yangtze River into the lake could alleviate deterioration of the water in the basin, improve the water environment, speed up the flow within the lake, improve the self-purification capacity, and shorten the water-change rate of the lake.<sup>2)</sup>

In this study, the flow and water quality in the lake in 2013 were simulated. By varying the artificial water diversion from the Yangtze River in the model, the effect of diversion on the water quality of the lake, especially in the northern region, where cyanobacteria outbreaks are severe, were studied. The purpose of the study is to clarify the impact of the Yangtze River diversion on the central and northern regions and propose an improvement of water diversion measures.

## 2. Materials and Methods

### 2.1 Description of the study area

Lake Taihu is the third largest freshwater lake in China. It is in the southern part of Jiangsu Province, adjacent to Zhejiang. It has an average water depth of 1.9 m, a maximum depth of 2.6 m, and a volume of 4.43 billion cubic meters. The average volume of water entering the lake annually is 5.72 billion cubic meters, and the water is changed every 317 days. Fig. 1 shows the location of the lake, and the river channels and water gates those used to divert water.



Fig. 1 Geographical location of Lake Taihu, river channels and water gates.

### 2.2 Methodology

In this study, a three-dimensional flow model developed by Zhang et al., semi-implicit cross-scale hydroscience integrated system model (SCHISM), is used with an unstructured grid. SCHISM solves the Reynolds averaged Navier–Stokes (RANS) equations and uses the Boussinesq approximation to approximate the transfer of heat, salt, and tracer in a hydrostatic form with unstructured simulation grids.<sup>3)</sup> In the vertical direction, a simple sigma grid was used in this study.

The water quality simulation in this study used the integrated compartment model (ICM) module coupled to the SCHISM model framework. It comprises 21 variables, including zooplankton, phytoplankton, organic carbon, nitrogen, phosphorus, silica, chemical oxygen demand, and dissolved oxygen (DO), etc.. The specific settings of the model and simulation are shown in Table 1.

Table 1 Setting and Conditions of the model.

|                     | Setting   |                            |
|---------------------|---|----------------------------|
|                     | Node space  | ca. 500 m                  |
| Horizontal Grid     | Number of grids                                     | 12690                      |
| Vertical Grid       | Number of layers                                    | 5 layers                   |
|                     | Coordinate system                                   | $\sigma$ coordinate system |
| Meteorological Data | Data from Climate Forecast System Version 2 (CFSv2) |                            |
| River Flow Data     | Lake Taihu Basin Administration                     |                            |
| Spin-up Period      | 2013.1.1–2013.5.31                                  |                            |
| Simulation Period   | 2013.6.1–2013.12.31                                 |                            |
| Timestep            | 120s  |                            |

## 3. Results and Discussion

### 3.1 Model reproducibility

The reproducibility of the model is mainly achieved by comparing the water temperature, ammonia nitrogen ( $\text{NH}_4\text{-N}$ ), total nitrogen (TN), phosphate ( $\text{PO}_4$ ), total phosphorus (TP), DO, cyanobacteria biomass and algae biomass ratio's calculated results of Case-R (using seasonal water diversion data same as reality) and observed values. The observation data are obtained from the Lake Taihu monitoring dataset.<sup>4)</sup> Locations for validation are the observation stations of THL01 and THL08, marked with red dots in Fig. 1. THL01 is in the northern Meiliang Bay, an area prone to cyanobacteria, and THL08 is located in the central area of the lake. The reproducibility of these two points is highly beneficial to the overall water quality research.

Fig. 2 shows the simulated TN, TP, DO, and cyanobacteria biomass at THL01 and THL08. The model has good performance during the study period when cyanobacteria blooms are prone to occur.

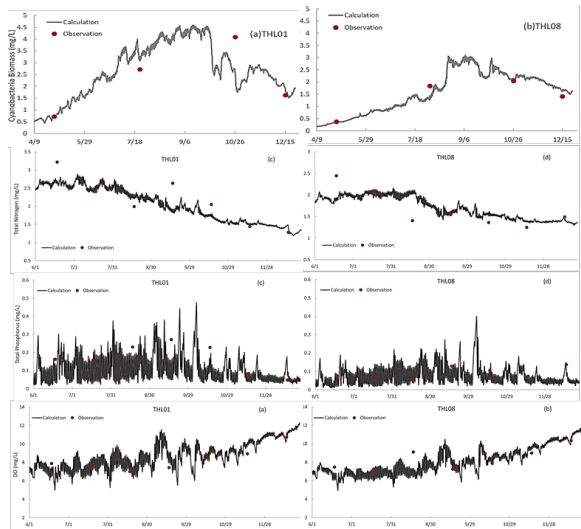


Fig. 2 Simulated TN, TP, DO, and cyanobacteria biomass at THL01 and THL08 of Case-R.

### 3.2 Impact of water diversion

Because Wangting and Taipu Watergates could be completely controlled, it is possible to manually adjust the amount of water drawn from the Yangtze River. This simulation varies the water diversion volume of the Wangting Watergate in 2013 by factors of 0, 0.25, 0.5, 0.75, 1.25, 1.5, 1.75, and 2 relatives to the reality value to observe the impact on the lake water quality.

Fig. 3 shows the average flow of Case-0 (no diversion), Case-R and Case-2 (2-fold volume) from Aug. to Sept. 2013. It can be seen that the impact of water diversion on the flow velocity is mainly concentrated in the northern part. It can be expected that the water diversion will improve the water quality of the northern part.

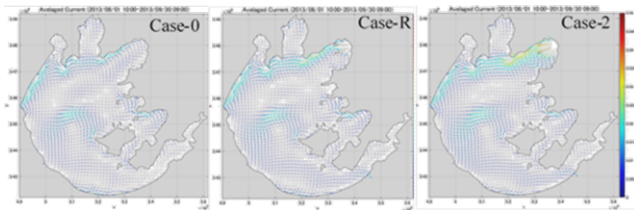


Fig. 3 The average flow of Case-0, Case-R and Case-2 from August to September 2013.

At THL01 the cyanobacteria biomass decreased with the increase of water diversion during August to October, and the gap between the cases gradually increased over time. In THL08, the cyanobacteria biomass grows relatively smoothly in Case-0 and as the water diversion volume increases, the fluctuation increases. Water diversion can reduce the TN concentration by about 0.3mg/L at most. This has a great impact on the lake, which has a target TN content of 2mg/L. In different cases, the results of TP and DO have not changed much and the results of TP and DO met the target value in all cases.

Fig. 4 shows the ratio of the averaged concentrations of each case to Case-R. To evaluate the impact of water diversion volume, the calculation results were averaged during Aug. to Oct. for each water diversion case, and find the ratio to the averaged value of Case-R.

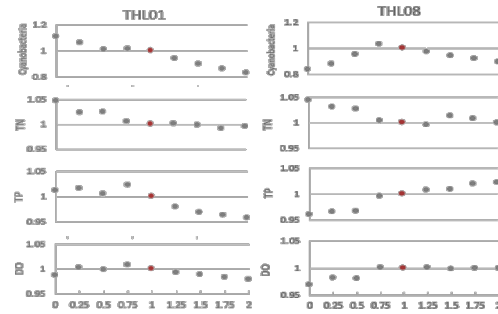


Fig. 4 The ratio of the averaged concentration of each case to Case-R from August to October.

At THL01, comparing Case-0.5 (0.5-fold volume) and Case-0, the cyanobacteria biomass decreased by about 10%. When the water volume rises to Case-2 level, it will be reduced by about 25%. In terms of TN and TP, water diversion can improve them slightly. A small amount of water diversion can increase the level of DO, while continuing to increase the amount, the DO will decrease. At THL08, the algae biomass in all cases was larger than that of Case-0. However, when the water volume exceeds Case-0.75, the biomass will fall again. Water diversion will increase the TN and DO levels, but when the amount of water conduction is larger than Case-R, the effect is no longer obvious.

In the calculation of the TN compliance rate from Aug. to Oct., water diversion has a significant impact on the improvement of TN in the northern part of the lake. Even a small amount of water diversion, such as Case-0.25, can increase the compliance rate from 38% to about 47%. When the water conductivity exceeds the Case-0.75 level, although the compliance rate has declined, it can still be maintained at about 51%. In the lake center, water diversion has little effect on the compliance rate, and the compliance rate in each case is around 85%.

### 4. Conclusions

(1) Seasonal water diversion is beneficial to improve the cyanobacteria outbreak in the northern part of Lake Taihu. (2) Even a small amount of water diversion can improve the condition of cyanobacteria and TN in the northern part of the lake. (3) Although DO and TP will deteriorate in central area due to the water diversion, they can still meet the standards. (4) It is possible improve the condition of cyanobacteria in the north by increasing the amount of water diversion. Even doubled the volume of diversion can still satisfy the water quality standards in the central part of the lake.

### References

- 1) Bai XH: Importation of wind driven drift of mat like algae bloom into Meiliang Bay of Taihu Lake in 2004 Summer. *J. Environ. Sci.*, **26**(6), 57–60, 2005. [In Chinese]
- 2) Hu WP: Study on the 3D numerical simulation of dynamics in Lake Taihu, China. 1. Wind-driven and the up and down of water level induced by wind. *J. Lake Sci.*, **10**(4), 18–25, 1998. [In Chinese]
- 3) Zhang YJ, Ye F: Seamless cross-scale modeling with SCHISM. *Ocean Model.*, **102**, 64–81, 2016.
- 4) Min C, Qian R et al.: 2007–2015 Taihu water body physical and chemical monitoring dataset. *China Scientific Database*, **5**(1), 2020.



# Numerical study on derivation of hydrodynamic coefficients of AUV using CFD based on N-S equation of non-inertial coordinate system

Chan Siyu

Naval Architecture and Ocean Engineering

**Key Words:** AUV, Non-inertial coordinate system, Forced oscillation test, CFD, OpenFOAM

## 1. Introduction

In recent years, ocean exploration has gradually been paid attention to by various countries, and some ocean exploration technologies have also been well developed. For example, Autonomous underwater vehicles, so known as AUV, are widely used in this area such as ocean resource exploration and ocean environment exploration.

To meet the requirements for different working conditions, the AUV design should take hydrodynamic performance as an important target. So firstly, the force condition for a sailing AUV should be studied. To know the force condition, computational fluid dynamics (CFD) is a good choice because of the relatively low cost and the feasibility. For example, GAO and PAN derived hydrodynamic coefficients of a high-speed AUV by using dynamic mesh tech. And Joung T., Sammut, K. did a study on the design optimization of an AUV by using computational fluid dynamic analysis.

But the dynamic mesh tech has its own disadvantages. Firstly, the efficiency is not good. The solving for mesh movement in every time step consumes a lot of computing resources which results in high time cost. Secondly, the numerical stability is not good. Calculations are usually tended to diverge.

So in this work, a new method is developed to derivate the force coefficients by describing the motion of the object in a non-inertial coordinate system. When the coordinate system is fixed on the object, the deformation and the displacement of the mesh system can be avoided fundamentally. By doing that, the efficiency of the simulation is greatly improved, and the numerical stability is also greatly made better. Besides, the accuracy is compared in this work. Two descriptions share the same trend in time history.

## 2. Basic equations of fluid mechanics in non-inertial coordinate system

To do the simulation in a non-inertial coordinate system, the basic equations of fluid mechanics should be set up in a non-inertial coordinate system. And firstly, the theorem for the composition of velocity and acceleration is known as:

$$\vec{u}_a = \vec{u}_r + \vec{u}_0 + \vec{\omega} \times \vec{r}_1 \quad (1)$$

$$\vec{a}_a = \vec{a}_r + \vec{a}_0 + \frac{d_0 \vec{\omega}}{dt} \times \vec{r}_1 + \vec{\omega} \times (\vec{\omega} \times \vec{r}_1) + 2\vec{\omega} \times \vec{u}_r \quad (2)$$

### 2.1 Continuity equation

Using relative velocity and acceleration instead of absolute velocity and acceleration, the continuity equation in a non-inertial coordinate system can get as:

$$\nabla \cdot \vec{u}_r = 0 \quad (3)$$

### 2.2 Momentum Equation

And also, the momentum equation can get as:

$$\frac{\partial \vec{u}_r}{\partial t} + (\vec{u}_r \cdot \nabla) \vec{u}_r = f - \frac{1}{\rho} \nabla p + \nu \nabla^2 \vec{u}_r \quad (4)$$

Where the source term  $f$  is:

$$f = -\left[\frac{d_0 \vec{u}_0}{dt} + \vec{\omega} \times (\vec{\omega} \times \vec{r}_1) + 2\vec{\omega} \times \vec{u}_r + \frac{d\vec{\omega}}{dt} \times \vec{r}_1\right] \quad (5)$$

The value of relative velocity  $\vec{u}_r$  is processed as the value of it in the previous time step.

## 3. Solver process

Based on the basic equations of fluid mechanics in non-inertial coordinate system, a solver is made by using PIMPLE algorithm. And the process is shown in Fig 1.

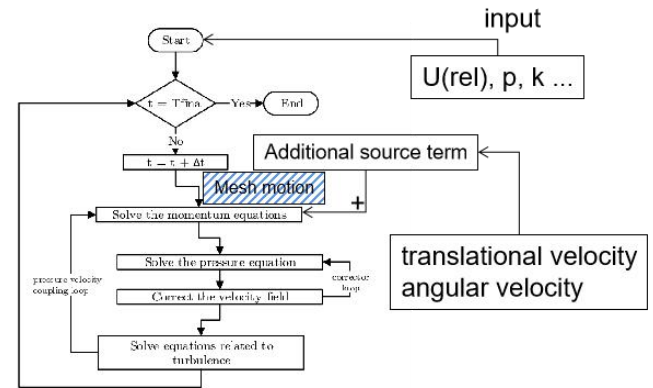


Fig 1 relPimpleFoam Process

The translational and the angular velocity are included in the additional source term contribute in every step of the calculation. So that the solving for the mesh motion is avoided.

## 4. Solver Correctness Verification

In order to compare the difference between the non-inertial coordinate system and the inertial coordinate system for fluid simulation. Two cases based on the same model, motion, fluid properties and turbulence parameters will be tested. The only difference is, motion is described in inertial coordinate system in one case and in non-inertial coordinate system in the other case.

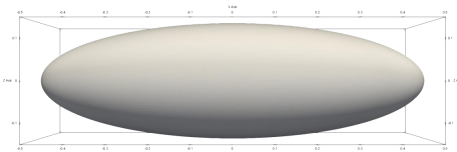


Fig 2 Model

### 4.1 Case settings

Table 1 Case Parameters

|                                |  |
|--------------------------------|--|
| Type of Fluid                  | Water (20 °C)                                    |
| Density                        | $998.2 \text{ kg/m}^3$                           |
| Kinematic Viscosity            | $1.002 \times 10^{-6} \text{ m}^2/\text{s}$      |
| Dynamic Viscosity              | $1.004 \times 10^{-3} \text{ Pa} \cdot \text{s}$ |
| Characteristic length of model | 0.212776 m                                       |
| Reynolds Number                | 105646.251                                       |
| k                              | $5.32325 \times 10^{-4} \text{ m}^2/\text{s}^2$  |
| $\varepsilon$                  | $1.35496 \times 10^{-4} \text{ m}^2/\text{s}^3$  |

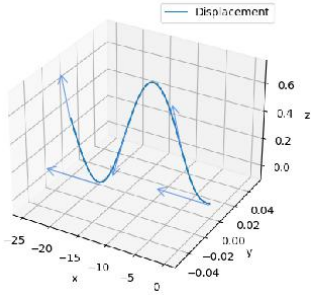


Fig 3 Motion

#### 4.2 Accuracy Analysis

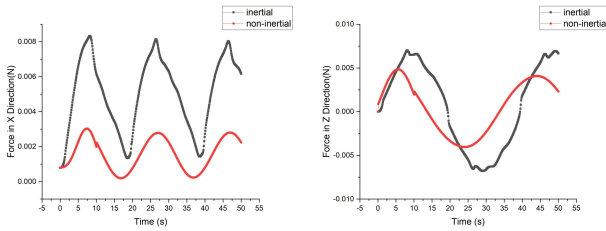


Fig 4 Force Analysis

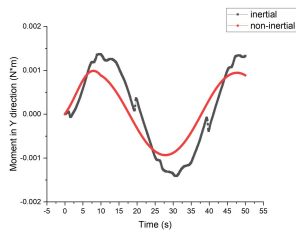


Fig 5 Moment Analysis

The force condition of the two reference systems is shown in Fig 3 and Fig 4. The motion is limited in the X-Z plane, so force in the Y direction and moment in the X and Z direction are ignored.

The force in the X and Z direction share the same trend in time history. And the moment in the Y direction matched very well.

#### 4.3 Efficiency Analysis

Table 2 Efficiency Analysis

|                                  |                 |
|----------------------------------|-----------------|
| CPU                              | AMD RYZEN 5950X |
| SMT                              | OFF             |
| Cores                            | 10              |
| Number of cells                  | 280,391         |
| Time cost in inertial system     | 3242s           |
| Time cost in non-inertial system | 663s            |

The calculation condition is shown in Table 2, by describing the motion in a non-inertial coordinate system, the time cost was reduced by 79.5 %. And as is shown in Fig 6, the numerical stability is much better in a non-inertial coordinate system.

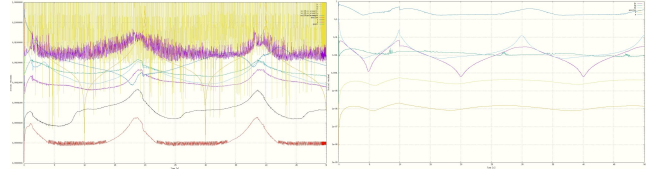


Fig 6 Residuals for inertial coordinata system (left)  
& for non-inertial coordinate system (right)

#### 5. hydrodynamic coefficients

After the correntness verifivation, the hydrodynamic coefficients is derivated. And the result is shown in Fig 7. Where the lift (Cl), the drag (Cd) and the moment (Cm) coefficients is measured and shown.

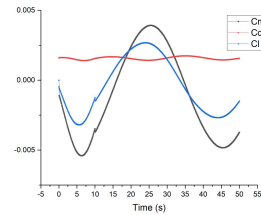


Fig 7 Time history of hydrodanamic coefficients

#### 6. Conclusion

In this paper, a non-inertial system-based fluid mechanics solution method is developed. And the accuracy and the efficiency of the method are analyzed. Two descriptions share the same trend in the time history of force condition. Besides, the efficiency and the numerical stability are much better by using the non-inertial system-based method.

#### References

- 1) Gao, F. D., Pan, C. Y., Xu, X. J., & Han, Y. Y. (2012). Numerical computation and analysis of high-speed autonomous underwater vehicle (AUV) moving in head sea based on dynamic mesh. Journal of Central South University, 19(11), 3084-3093.
- 2) Joung, T., Sammut, K., He, F., & Lee, S. K. (2009, July). A study on the design optimization of an AUV by using computational fluid dynamic analysis. In The Nineteenth International Offshore and Polar Engineering Conference. OnePetro.

# An Investigation on Patch Welding Repair for Thickness Reduction of Steel Structural Compressive Member

CHENG Yuxuan

Structural Engineering Laboratory, Department of Civil Engineering

**Key Words:** Welding, Repair, Thickness reduction, Load-carrying capacity, Finite element method

## 1. Introduction

When applying patch plate to thickness-reduced steel bridge members due to corrosion, high-strength bolts are generally selected as the joining method, and welding is rarely used [1]. In this study, considering the adaptability of repair by patch welding on thickness-reduced steel structural members, a basic experiment and its numerical simulation were conducted to examine the effect of patch welding in each different dimension. The changes in compressive behavior of thickness-reduced steel structural member repaired by different dimensions of patch plates were examined.

## 2. Compressive Experiment

### 2.1 Size design of patch plate specimen

In this study, in order to clarify the influence of dimension of patch plate on the ultimate strength of patch-repaired specimen, steel plate specimens with uniform thickness reduction were fabricated.

The length of the thickness-reduced base plate is always 600 mm. The length of thickness reduction is 60 mm. The thickness reduction of base plate is 50% [2] of the original thickness as 18 mm. As shown in Table 1, the length of patch plate,  $L$  is 90 mm in A, B and C specimens. That is 150 mm in D, E and F specimens. The thickness of patch plate,  $t_p$  and the weld bead size,  $s$  are different in each group. The number of specimens in each group is 3.

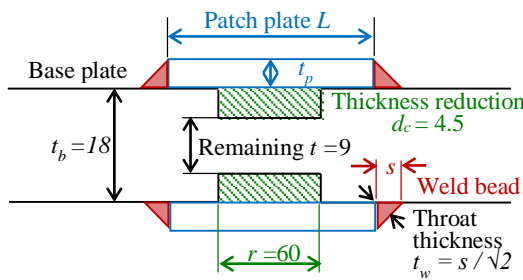


Fig. 1 Shape and dimension of specimen (mm)

Table 1 Detailed size information of specimens (mm)

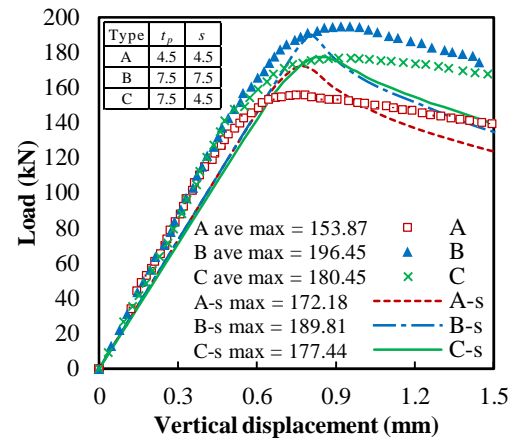
| Type | $t_b$ | $t$ | $L$ | $t_p$ | $s$ |
|------|-------|-----|-----|-------|-----|
| A    | 18    | 9   | 90  | 4.5   | 4.5 |
| B    | 18    | 9   | 90  | 7.5   | 7.5 |
| C    | 18    | 9   | 90  | 7.5   | 4.5 |
| D    | 18    | 9   | 150 | 4.5   | 4.5 |
| E    | 18    | 9   | 150 | 7.5   | 7.5 |
| F    | 18    | 9   | 150 | 7.5   | 4.5 |

### 2.2 Experimental condition

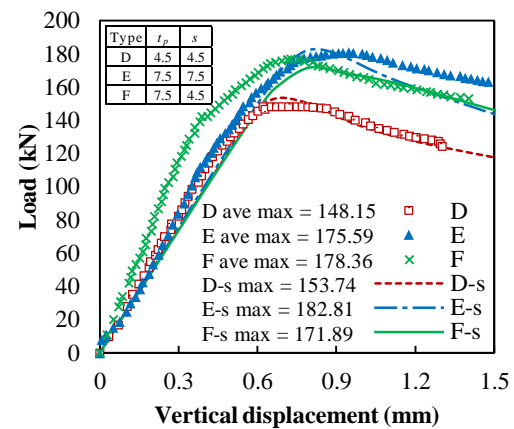
After measuring and recording the detailed dimensions of each specimen, a universal testing machine was used for the compressive loading experiment on the 6 sets of specimens. The

specimens were fixed on both ends by steel blocks. Two displacement transducers were set between the upper and lower blocks for measuring the vertical displacement.

By the loading machine, the monotonic compressive load in a vertical direction was slowly applied to the specimen. The maximum load was confirmed and the vertical displacement reached 2 mm, then the load was released. Fig. 2 shows the relationship between load and vertical displacement. In the figure, the result of one specimen per each group is shown.



(a) Load and vertical displacement of A, B, C



(b) Load and vertical displacement of D, E, F

Fig. 2 Results of compressive loading experiments

## 3. Elastic Plastic Analysis

### 3.1 Analysis model information

As one of the highlights of this study, we performed an elastic-plastic analysis to verify the results of the experiment. At the same time, the compressive behaviors of the intact model, the corroded thickness-reduced model, and the patch-repaired model are compared.



In order to keep consistent with the experimental conditions, the simple and easy-to-use models are used in this analysis, with a uniform, constant thickness reduction and initial deformation of model surface. Also due to the relatively slender and long size of the steel structure component and its symmetry, the deformation under force is mainly bending deformation, we ignored its slight deformation on the width direction, two-dimensional plane strain condition simulation was chosen, as shown in Fig. 3. In the experiment, materials of specimens did not experience significant temperature changes so that we picked the curve is the characteristic of the steel material at 0 degrees Celsius [3].

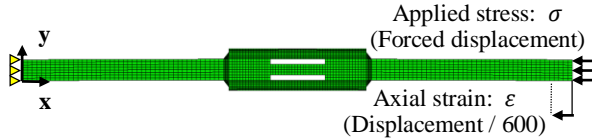


Fig. 3 Simulation model and mesh division.

### 3.2 Analysis simulation results

After analysis simulation, we got the maximum load value of the intact model was 185.13 kN. We take it as the target bearing capacity on others patch-repaired models.

The simulation results for experiments are shown by continuous lines in Fig. 2, and we could think the simulation curves and results are basically in line with the experimental curves and results.

In the A, B, C groups, the simulated maximum load of A is 172.18 kN, which is 11.90% higher than the experimental average result. The simulated maximum load of B and C are more consistent with the experiment. They are 3.38% and 1.66% smaller than the average of the experimental results, respectively.

In the D, E, F groups, D specimens and the E specimens made were unqualified, because holes are created in weld bead connection part due to poor welding, which made the simulated maximum load of D and E are much higher than the experimental average results values. But when we added 4 holes in each model, the simulation results are closer to the experimental results, which were only 3.78%, and 4.11% higher than the experimental average values. And in E group, it is 3.63% lower than the experimental average value. As shown in Fig. 4.

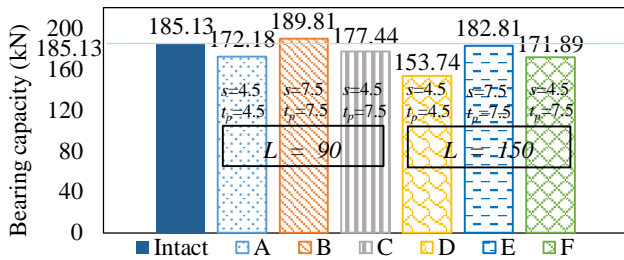


Fig. 4 Analysis simulation results on different models

## 4. Analytical study of patch welding repair on thickness-reduced structural member subjected to compressive loads

### 4.1 Analysis model basic information

Because the analysis of the previous Chapter Three is only aimed at six kinds of simulation analysis. In this part, we hope to conduct

more simulations to explore the recovery of the repaired patch-plate load performance under different parameter conditions. We selected materials and analysis condition which the same as the experiment used and the previous simulations used.

This time, we simulated the specimens under 75 different conditions to obtain the maximum load-bearing stress under the different conditions. We still selected the test specimens with the corrosion amount in the center part of the test specimens being 50% of the original thickness, and selected the weld bead size equal to 4.5 mm, 6.0 mm, 6.5 mm, 7.5 mm, 9.0 mm. After that, we selected the thickness of the patch plate according to the bead size which larger than the bead size. Finally, we set the length of patch plate to 60 mm, 90 mm, 120 mm, 150 mm, 180 mm.

### 4.2 Simulation results

When the weld bead size  $s$  were 4.5 mm and 6 mm, the maximum load stress did not reach the target load stress 185.13 kN. When the weld bead size  $s=6.5$  mm, the maximum load stress reached the target stress in some cases. It is considered that this is because the throat thickness  $t_w$  (When  $s=6.5$  mm,  $t_w=4.6$  mm) is almost equal to the thickness reduction on one side of base plate  $d_c$  (4.5 mm). When the weld bead size  $s$  were 7.5 mm and 9 mm, the maximum load stress was higher than the target stress except the situation with patch plate length  $L=60$  mm. At the same time, the patch plate was longer the maximum load stress was higher.

Based on the deformation modes obtained by the simulation, bending of patch plate occurs at the welded ends of the patch plate. This bending deformation was restrained due to the contact between the patch plate and the base plate when the patch plate length was long enough. In this study, it was suggested that the patch plate length should be longer by 30 mm than the thickness-reduced region.

## 5. Conclusions

(1) Whether in experiments or analysis simulations, the ultimate compressive strength of thickness-reduced steel plates with patch welding was influenced by the weld bead size and the thickness of patch plate.

(2) Under the limited conditions performed in this study, it is not that the longer patch plate will provide greater ultimate strength, the shorter patch plate provided the higher ultimate strength.

(3) In order to restore the load bearing performance to the target stress level (the maximum load stress of the model without the backing plate also without thickness reduction), we should ensure that the throat thickness is greater than or equal to the base plate thickness reduction, and set the length and thickness of the patch plates corresponding to throat thickness. Throat thickness of bead size was a dominant factor.

(4) Through many simulations, we can infer that the length of the patch plate should be set to be about 30 mm longer than the thickness-reduced area.

## References

- 1) Gheitasi, A., & Harris, D. K. (2015). *Journal of Bridge Engineering*, 20(3), 05014012.
- 2) Tamakoshi, T., Yoshida, Y., Sakai, Y., & Fukunaga, S. (2006). *Public Work Research Institute of Japan*.
- 3) 中川弘文, & 鈴木弘之. (1999). *鋼構造論文集*, 6(22), 57-65.

# Investigating users' acceptance on battery-swapping electric two-wheelers

Kanbei Shi

Transportation and urban design, Civil engineering

**Key Words:** Battery sharing service, E2W, motivation, lifestyle, path analysis

## 1. Introduction

Transportation electrification<sup>[1]</sup> is proposed and regarded as one of significant opportunities to address harmful effects caused by overreliance on mass motorization. However, even great efforts have been taken in promoting electric vehicles and restricting conventional vehicles by government worldwide, mass adoption of electric vehicles has been hampered by many factors such as limited driving range, insufficient charging infrastructure<sup>[2]</sup>. Battery swapping system was proposed and provided a solution through providing battery share or subscription service instead of selling. In Japan, E2W stays in low acceptance levels. After the outbreak of Covid-19, battery swapping electric two-wheelers (BS-E2W), as a convenient eco-friendly mobility with hedonic quality in usual days, offer a low-infection-risk means of commute and leisure activities in unusual days. On the other hand, E2W is relatively vulnerable road participants, its promotion needs careful consideration of emerging safety issues.

This study aims to find factors that influence user's acceptance on BS-E2W, and to explore how those factors influence consumers' intentions switching between purchase intention and intention to use battery sharing service.

The research structure is organized as follows. Chapter 1 describes the background and the aims of this research. Chapter 2 presents a review of the literature on factors in relation to users' acceptance of BS-E2W and proposed the research hypothesis. Chapter 3 describes the details of survey context, questionnaire design, and data analysis methods. Chapter 4 presents the results of data analysis and the outcome of path analysis models. Chapter 5 discusses the findings and limitation of this research.

## 2. Literature review

### 2.1 Factors influencing acceptance of BS-E2W

Previous literature inspired us that instrumental, hedonic, value-rational motivation, concerns may influence the user's lifestyle and further influence their usage intention to E2W.

### 2.2 Research hypotheses

Based on literature, an exploratory model (see Fig. 1) of factors influencing usage intention was presented. First block of variables that extracted from pre-questionnaire include instrumental, hedonic, value-rational motivation, and concerns, working as exogenous variables, which are also expected to have direct effects on satisfaction and usage intention. Post perception and concerns are expected to mediate the relationship between motivation and usage experience and lifestyle change. The second block variables would directly predict satisfaction and usage intention, mediating the effects of motivation.

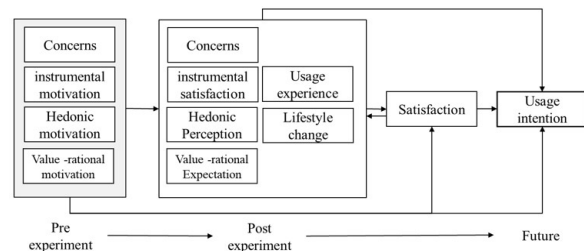


Fig. 1 Hypothesized conceptual model

## 3. Methods

### 3.1 Survey

The demonstration experiment "Eyan Osaka" is conducted by the Japan Automobile Manufacturers Association in cooperation with Osaka local government, Osaka University, and Lawson convenience stores. In the project, experimental-use E2Ws (see Fig. 2) were rented to participants at a price of 1000 JPY per month. 12 battery swapping stations (1 in Suita campus, 1 in Toyonaka campus, 10 in convenience stores, see Fig. 2) have been set up within the Hokusetsu area. The program last one year from September 2020 to October 2021, four phases in total. The 10 battery swapping stations in convenience stores were put into use in the second phase. Until the completion of this research, the project has collected all data of 2 phases.



Fig. 2 Electric two wheelers, swappable battery, battery swap station, stations in convenience store (left to right)



Fig. 3 Photos of safety training

### 3.2 Sample, procedure, data analysis

In this study, we focused on students and faculty in Osaka university. In each phase of experiment, participants were asked to fill 3 online questionnaires and attend online group interview (see Table.1). Subjective questionnaires and objective usage data were collected to explore how hypothesized factors affected respondents' acceptance on BS-E2W. Demographic attributes were collected from recruitment questionnaire, motivation-related questions were asked in pre-questionnaire while questions of perception, satisfaction, intention and usage behaviors were in the post questionnaire. Except the questionnaire data, we collected

usage data from sensors on vehicles like origin-destination, monthly battery swapping times, trips, driving distance. The responses from questionnaires and usage data from sensors were analyzed on statistical analysis software IBM SPSS 23.0 and Amos 24.0.

Table. 1 Summary of survey

|               |  |
|---------------|--|
| Survey method | Three online questionnaires (recruitment, pre, post);<br>Online group interview                    |
| Survey time   | Phase I: 2020.9.27- 2020.12.31<br>Phase II: 2021.1.15- 2021.3.31<br>※2021.1.11: C-BSS put into use |
| Target group  | University students and faculty  |
| Sample size   | Phase I: 21 (2 professors)<br>Phase II: 11 (1 staff)<br>32 in total                                |

## 4. Results

### 4.1 Descriptive statistics

32 participants were recruited in the study and completed all of questionnaires. 28 males and 4 females, with a mean age of 22.3. 65.5% were undergraduates, followed by 25.0% graduates and 9.4% faculty. 53.1% of respondents' commute mode were active walking and cycling, 12.5% was powered two-wheelers (PTW), 31.1% was public transport. Except 34.4% experienced PTW riders, the rest of participants were beginners not only E2W but also PTW.

### 4.2 Difference analysis

T test results showed participants' value-rational expectation (environmental and altruistic) increased and realized high-price attribute of E2W after participation. Male participants were more particular about instrumental attributes of E2W, while female respondents were easily satisfied and perceived higher environmental awareness. Participants who had driven E2W for last mile showed higher post instrumental satisfaction, comprehensive changes in their lifestyle not only in weekday but also in weekend activities. This group presented significantly higher general satisfaction and higher usage level.

### 4.3 Correlation analysis

From the calculation of spearman's rho correlation coefficients matrix, general satisfaction "BS-E2W fits my life", were positively correlated with hedonic perception, lifestyle items on "increased freedom of university-related activity" "expanded range in weekday", "increased communication with friends", monthly trips, while negatively correlated with post service concerns "troublesome process of battery swapping".

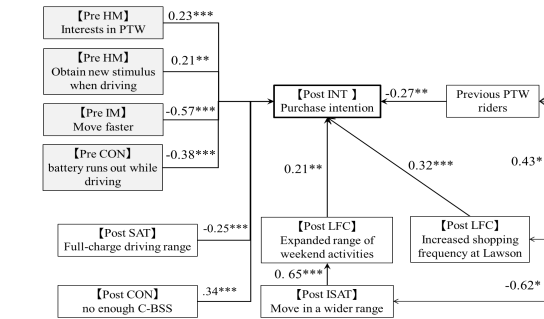
### 4.4 Path analysis

Path analysis is a powerful statistical technique that allows for more complicated models than multi-regression model, it can examine "chains" of influence between exogenous variables and endogenous variables.

In this section, two path analysis models were constructed and estimated including all path coefficients, significance and goodness-of fit. Considering the limited samples, the overall model fit was acceptable.

The results of 1<sup>st</sup> path model (CMIN/DF= 1.114,  $p = 0.281$ , RMSEA= 0.077, GFI=0.714, CFI=0.923) shows people who show higher purchase intention (1) care much about hedonic

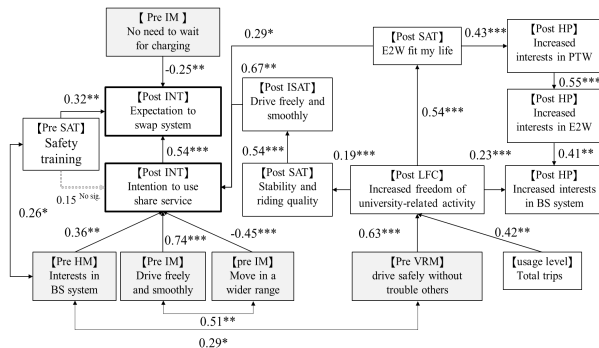
attributes of E2W, whereas instrumental dissatisfaction may reduce the intention; were dissatisfied with the BSS location and driving range in this experiment; (3) tend to drive for activities on weekend instead of daily commute; (4) experienced motorcycles have a relatively lower willingness to purchase possibly because of limited driving range of E2W.



$p < 0.001$ \*\*\*,  $p < 0.01$ \*\*,  $p < 0.05$ \*

Fig. 4 Path analysis on purchase intention N=20

The results of 2<sup>nd</sup> path model (CMIN/DF= 1.151,  $p = 0.143$ , RMSEA= 0.070, GFI=0.728, CFI=0.907) indicates that people who had higher intention to use share service (1) highly motivated by instrumental expectation/ satisfaction, interest about new BS system; (2) did not expect to move in a wide range (narrow driving range is enough) (3) tended to drive for university-related activities in weekday. In addition, it is worth mentioning that safety training not only taught users safely-driving skills but also positively correlated participants' interests in the BS E2W and directly influenced users' anticipation to swap system



$p < 0.001$ \*\*\*,  $p < 0.01$ \*\*,  $p < 0.05$ \*

Fig. 5 Path analysis on intention to use share service N=32

## 5. Conclusions

Value-rational (environmental and altruistic) expectation increased after experiment. Different demographic attributes groups and their usage purpose perceived different hedonic perception, satisfaction level and ideal form of acceptance for BS-E2W. Compatibility of participants' lifestyle play a significant role in this process. Extra information of service allows people faster adaption to this new system. Operators and policymakers should take efforts to bridge the information gap and actively address concerns of potential (but still hesitant) users how E2W and BS service might fit their daily life.

## References

- Mingfei B, Jilai Y: G of EM, 44-54, 7(3), 2018
- T. Eccarius, C.C. Lu.:J :J of ST, 215-231 14(3),2020

# Residual Stress in Wire and Arc Additive Manufacturing Using Low Transformation Temperature Material 10Cr-10Ni

HUANG WENJIA

Mathematical Modeling and Computational Analysis Lab,  
Naval Architecture and Ocean Engineering

**Key Words:** Wire and arc Additive Manufacturing, Low Temperature Transformation Material, Residual Stress, Contour Method, Finite Element Method, Numerical Simulation

## 1. Introduction

Additive manufacturing (AM) is a technique which build up objects layer by layer. Comparing to the conventional subtractive manufacturing methods, additive manufacturing technologies commonly apply wire or powder as a feedstock which is melted by a focused heat source and consolidated in subsequent cooling to form a part [1]. During past thirty years, with the advantage of saving material and time as well as facilitating the manufacture of complex assemblies formerly made of many subcomponents, additive manufacturing has become a hot issue in forming filed [2]. Additive manufacturing methods can essentially be divided into the nature and the aggregate state of the feedstock as well as by the binding mechanism between the joined layers of material [3]. The most popular processes for AM of metals are Laser Beam Melting (LBM), Electron Beam Melting (EBM), Laser Metal Deposition (LMD) and Wire and Arc Additive Manufacturing (WAAM).

Since additive manufacturing has been widely applied to fabricate functional metal parts in a variety of industries. The requirements for component performance are also getting higher and higher. Due to the unique thermal cycle of metal additive manufacturing which is characterized by the rapid heating, cooling rates and re-melting of underlying previously solidified layers, residual stress is generated. On one hand, parts' fatigue life will be reduced by tensile residual stress. On the other hand, steep residual stress gradients will cause deformation which will decrease shape accuracy [4,5]. To solve these two points, researchers in National Institute for Material Science applied a classic low transformation temperature material 10Cr-10Ni as deposition material [6,7].

In their research, it was clearly approved by experiment and numerical simulation that the deformation can be efficiently decreased through using low transformation material. However, for residual stress, only contour method measurement was performed. At present, there is no effective explanation for this problem from the perspective of numerical simulation.

## 2. Theory

### 2.1 Thermal Elastic Plastic Analysis

In this paper, a simplified hemisphere shape and Gaussian function given by Eq. (2.1) are employed. The heating zone is shown in Fig.2.1.

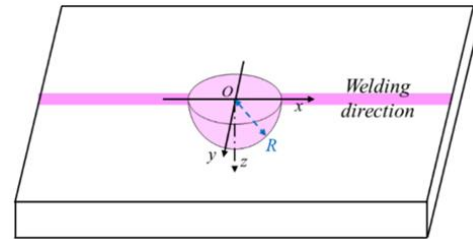


Fig. 2.1 Heat source model and heating zone.

$$q_V = \frac{3Q}{2\pi R^3} \exp \left[ -3(x^2 + y^2 + z^2)/R^2 \right] \quad (2.1)$$

Where, the R and x, y, z are the radius of a hemisphere of heating zone and moving local coordinates in which the origin is the welding arc centre located on the plate surface.

### 2.2 Contour Method

The Contour Method theory is based on Bueckner's elastic superposition principle. The diagram in Fig.2.2 shows the initial residual stress distribution acting in the horizontal direction in a given structure (step A). The plate is cut into two parts along the plane of interest (step B). This causes the cut faces to deform elastically due to the relaxation of residual stress. The resulting deformations (the contours) are measured using a surface profiling device with sufficient resolution (step C). After processing the data (step D), the virtual stresses required to 'force back' the deformed surfaces to their original shape are calculated (Step E). The results given in step F represent the initial stress distribution from step A acting normal to the plane of interest.

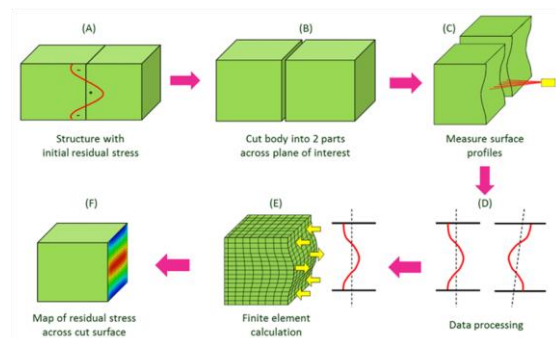


Fig. 2.2 Diagram of contour method for residual stress measurement.

## 3. Experiment

There are two different print shapes in this research. One is wall type which we call WAAM-I. The other one is pipe type which we call WAAM-O.



To use contour method, we need to use wire cutting to cut out the section to be measured. In this process, broken wires will have a great impact on the accuracy of the measurement results, so the operator must ensure the continuity of the cutting process as much as possible. The cut section can be directly used for measurement without any processing. The cutting and measured section of this experiment are shown in the Fig.3.2, and the measured section is on the symmetry plane.

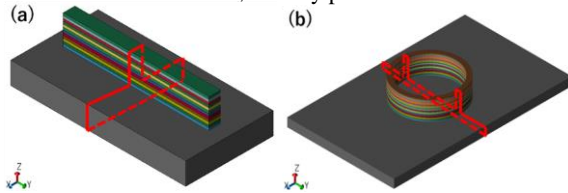


Fig. 3.1 Contour method measured section:  
(a) WAAM-I, (b) WAAM-O.

## 4. Numerical Simulation Results and Analysis

### 4.1 WAAM-I

The stress and strain analysis is also carried out by JWRIAN-HYBRID. Here we mainly discuss the residual stress along the welding direction, which means component of residual stress in Y direction in WAAM-I. Or we call it longitudinal residual stress. The calculation results of SUS308 case, LTT case and experiment measurement results are shown Fig.4.1-4.2.

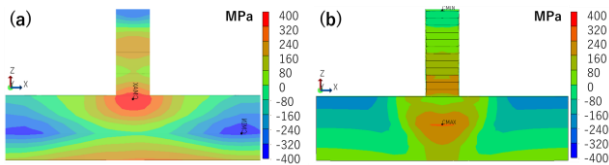


Fig.4.1 The results of SUS308 case:(a) Contour method measurement results, (b) Section surface simulation results.

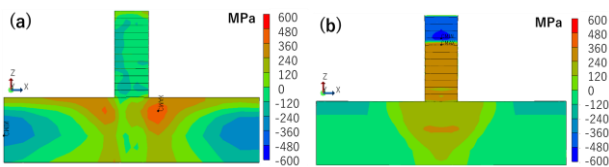


Fig.4.2 The results of LTT-10Cr10Ni case:(a) Contour method measurement results, (b) Section surface simulation results.

### 4.2 WAAM-O

The stress analysis is also performed by JWRIAN-HYBRID. The results of longitudinal residual stress and contour method measurement results are shown in Fig.4.3-4.4.

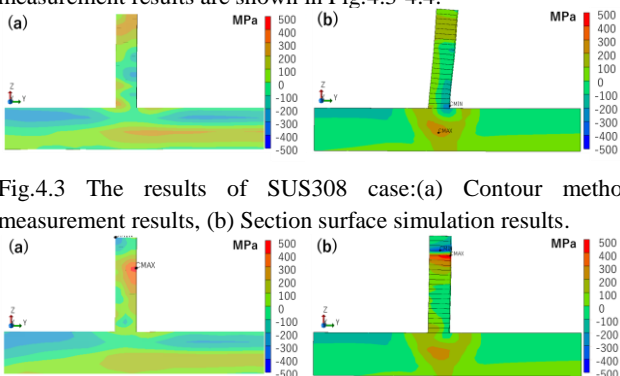


Fig.4.3 The results of SUS308 case:(a) Contour method measurement results, (b) Section surface simulation results.

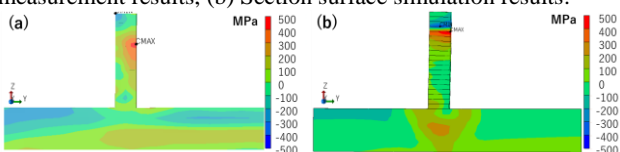


Fig.4.4 The results of LTT-10Cr10Ni case:(a) Contour method

measurement results, (b) Section surface simulation results.

## 5. Conclusions

The accuracy of the wire cutting experiment has a great influence on the measurement of residual stress using contour method. Measuring on a section that is partially damaged due to broken wires will make the measurement result difficult to judge and have large errors.

Through experiments, it is found that the first few layers in the additive manufacturing process are mutually diluted with the substrate. The change of material composition caused by this phenomenon will lead to the change of martensite transformation temperature for LTT, which in turn changes the properties of LTT material.

JWRIAN-HYBRID can accurately predict the residual stress distribution of the non-transforming austenite stainless steel SUS308 additive model WAAM-I and WAAM-O. For the phase transformation material LTT-10Cr10Ni, JWRIAN-HYBRID can also use the thermal expansion coefficient to perform a more accurate prediction of the phase transformation of the material. Finally, the two models, WAAM-I and WAAM-O, are basically consistent with the experiment measurements of residual stress distribution.

Under the working condition of multiple decreasing thermal cycles, LTT material cannot exert its characteristic of generating compressive residual stress through martensitic transformation at low temperature. Therefore, in multi-pass welding or multi-layer additive manufacturing, only the top layers can generate residual compressive stress. This is partly inconsistent with the original intention of reducing residual stress by using LTT materials for welding arc additive manufacturing. Therefore, the next work should be to consider how to make the LTT still produce compressive residual stress under the condition of multi-thermal cycles to improve the fatigue performance.

## References

- 1) Dirk Herzog, Vanessa Seyda, Eric Wycisk, Claus Emmelmann, Additive manufacturing of metals, Acta Materialia, Volume 117, 2016, Pages 371-392, ISSN 1359-6454.
- 2) Beaman Joseph J and Deckard Carl R, Selective Laser Sintering With Assisted Powder Handling, 1990-07-03, <https://lens.org/119-984-865-808-739>.
- 3) Kruth, J-P., et al. "Binding mechanisms in selective laser sintering and selective laser melting." Rapid prototyping journal (2005).
- 4) Shiomi, M., et al. "Residual stress within metallic model made by selective laser melting process." CIRP Annals 53.1 (2004): 195-198.
- 5) 北野 萌一, 中村 照美, 低変態温度溶接材料を用いた溶融金属積層造形材の変形低減法に関する基礎的検討, 溶接学会論文集, 2018, 36 巻, 1 号, p. 31-38.
- 6) Mercelis, Peter, and Jean - Pierre Kruth. "Residual stresses in selective laser sintering and selective laser melting." Rapid prototyping journal (2006).
- 7) S. W. Williams, F. Martina, A. C. Addison, J. Ding, G. Pardal & P. Colegrove (2016) Wire + Arc Additive Manufacturing, Materials Science and Technology, 32:7, 641-647.



# Effect of horizontal plates on the sliding of breakwater caissons

Sila Mercedes Fundora Campos

Coastal Engineering Laboratory, Department of Civil Engineering

**Key Words:** breakwater caisson, horizontal plate, sliding distance, performance design, BPS method

## 1. Introduction

Climate change is leading to an increase in frequency and intensity of natural disasters and a sea-level elevation, which threatens the stability of coastal protection structures. Furthermore, recent disasters have exposed the catastrophic damage to the land and port facilities that the destruction of such structures can cause. This fact implies that the loss of the structure's functionality influences the extent of damage in the area to be protected. Hence, evaluating the degree of functional deterioration of the structure at the time of failure ("performance at failure") is becoming essential.

Among coastal protection structures, vertical caisson breakwaters have been widely utilized. Most cases of breakwater damage involve sliding as a failure mode. Also, due to a combination of increases in sea level and wave height, sliding distances of caisson breakwaters are expected to become five times greater than at present, according to Takagi et al. (2011). Caisson (upright part of the breakwaters) can maintain their functionality even if a limited amount of sliding occurs. Sliding is not generally allowed under traditional breakwater design. Its stability has been conventionally judged using safety factors, balancing external and resisting forces. However, deformation parameters such as the sliding distance directly indicate their stability performance. Some researchers have been proposing "deformation-based reliability" design methods, such as Aoki et al. (1995)<sup>1</sup> and Shimosako and Takahashi (2000), or developing devices to extend such breakwaters functionality.

Present research pretends to contribute to the study of the caisson breakwaters' performance during the failure process by developing a reliable design method and describing the effectiveness of introducing horizontal plates to reduce the sliding motion of caissons. Such structure proposal is based on the hypothesis that a horizontal plate will increase the water constriction during the movement of the caisson, increasing the added mass and, in consequence, decreasing the expected sliding distance. The hypothesis was introduced and 'partially' proved in Yoshihara (2017, 2019)<sup>2</sup> with a 20% reduction of the sliding for a plate length  $l$  equal to the water depth  $h$ . However, it only considered the horizontal force in the analysis. Therefore, this study aims to evaluate the vertical forces introduced by the plate addition determining its influence on the sliding reduction accurately. Furthermore, to identify improvements and future research opportunities in caisson shape optimization is also pursued.

## 2. Methodology

The structure consists of a breakwater caisson with a horizontal plate located at sea level. In the model representation (Fig. 1), the water area is divided into three regions based on their different boundary conditions. The acting forces are also represented,

where  $F$  is wave force,  $F_R$  reaction forces, and  $F_f$  frictional force.

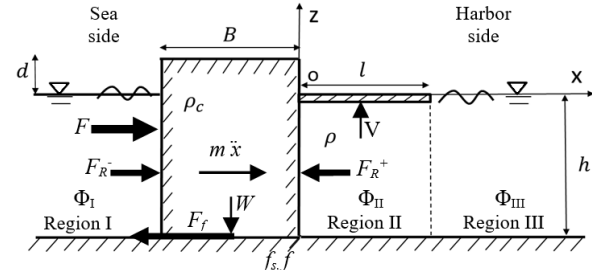


Fig. 1 Breakwater with a horizontal plate.  
Model representation

Linear wave theory, wavemaker theory, and potential theory are applied in the creation of a model which, after the introduction of a "boundary-points selection" method<sup>3</sup>) to determine velocity potentials, leads to the sliding calculation following the method proposed by Aoki et al. (1995)<sup>1</sup>.

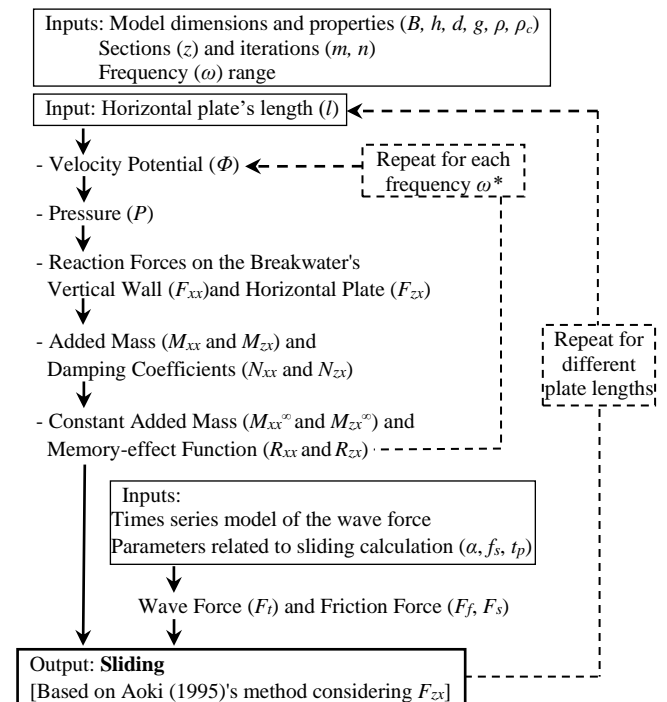


Fig. 2 Sliding calculation flow.

### 2.1 Velocity Potential. Boundary-Point Selection Method.

After applying boundary conditions, velocity potential solutions for regions I, II, III, are expressed by Eq.1, 2, and 3, respectively.  $A^+$  and  $B_n^+$  are known coefficients, and  $C_0$ ,  $C_m$ ,  $D_0$ ,  $D_m$ ,  $A^-$  and  $B_n^-$  unknowns. Eq.1 and Eq.3 are general expressions for velocity potential, while Eq.2 is derived after some mathematical procedures (Fourier expansions and transforms). Regions I and II share a boundary in  $x=l$ . In there, additional

$$\begin{aligned}\phi_I(x, z) &= A^+ \cosh k(z+h) e^{ik(x+B)} \\ \phi_{II}(x, z) &= \frac{1}{h} (C_0 + D_0 x) + \sum_{n=1}^{\infty} B_n^+ \cos k_n(z+h) e^{k_n(x+B)} \\ &\quad + \frac{2}{h} \sum_{m=1}^{\infty} \left\{ \left( C_m \cosh \frac{m\pi}{h} x + D_m \sinh \frac{m\pi}{h} x \right) \cos \frac{m\pi}{h} (z+h) \right\}\end{aligned}\quad (1)$$

$$\phi_{III}(x, z) = A^- \cosh k(z+h) e^{-ik(x-L)} \quad (2)$$

$$+ \sum_{n=1}^{\infty} B_n^- \cos k_n(z+h) e^{-k_n(x-L)} \quad (3)$$

conditions should be satisfied that grant the continuity of the velocity potential and its derivative. A practical method in which points at the shared boundary are selected and utilized to obtain an equation system with an equal number of equations and unknowns is proposed. The method is called the boundary-point selection method (BPSM), although it has been named in various forms<sup>3)</sup>. BPSM simplifies theoretical formulations and computer programming. Its accuracy is examined by comparing the results with the conventional method for an RMSE inferior to 1.E-03 by selecting 20 points.

## 2.2 Sliding

The equation of motion is expressed as Eq.4, where  $M_{xx}^\infty$  is the added mass at an infinite frequency, and  $R_{xx}$  is the memory-effect function used in Cummings (1962). The wave force  $F(t)$  in the time domain is determined by a triangle-shaped profile used in Aoki et al. (1995)<sup>1)</sup>.

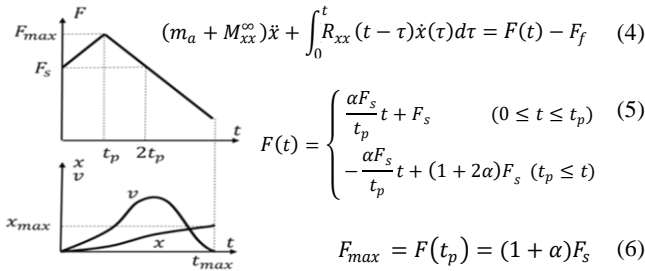


Fig. 3 Wave force and sliding models.

With the addition of the plate, uplift forces are more influential in the system. Thus, the vertical added mass  $M_{zx}^\infty$  and  $R_{zx}$  from those forces are introduced in the motion equation as part of the friction force. Static frictional force  $F_s = f_s W$  and dynamic frictional force  $F_f = f_d(W-V)$ , where  $f = f_s$  and the vertical force is expressed by Eq.7. Hence, the final equation of motion is defined by Eq.8.

$$V = -M_{xx}^\infty \ddot{x} - \int_0^t R_{xx}(t-\tau) \dot{x}(\tau) d\tau \quad (7)$$

$$(m_a + M_{xx}^\infty + f_s M_{zx}^\infty) \ddot{x} + \int_0^t [R_{xx}(t-\tau) + f_s R_{zx}(t-\tau)] \dot{x}(\tau) d\tau = \begin{cases} \alpha \frac{t}{t_p} F_s & (0 \leq t \leq t_p) \\ \alpha \left( 2 - \frac{t}{t_p} \right) F_s & (t_p \leq t) \end{cases} \quad (8)$$

## 3. Results and Discussion

The horizontal plate influence is analyzed by changing the ratio of plate length to water depth  $l/h = 0, 0.25, 0.5, 0.75$ , and  $1.0$ ; been  $l/h = 0$  the case of a caisson without a plate. For better evaluation, dimensionless analysis is made. Horizontal and vertical parameters are analyzed at  $x=0$  and  $z=0$ , respectively.

Added mass (Fig.4a) increases as the plate becomes larger, and it is asymptotic to a particular value  $M_{(\omega \rightarrow \infty)}$ . The ratio  $M_{zx}/M_{xx}$

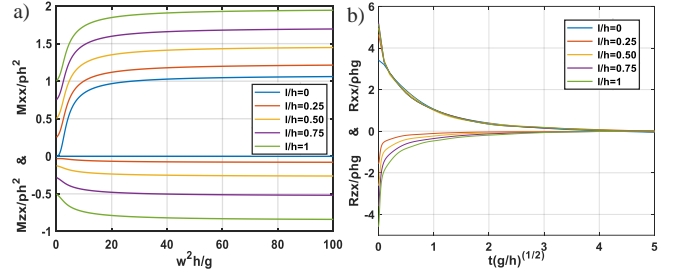


Fig. 4 a) Dimensionless added mass ( $M_{xx}$  and  $M_{zx}$ )  
b) Dimensionless memory-effect function ( $R_{xx}$  and  $R_{zx}$ )

risers for larger plates. Similar relations are seen in the memory-effect functions (Fig.4b). The longer the plate, the more equals become the parameters at the vertical wall and the horizontal plate. Thus, the plate works as an equalizer for horizontal and vertical directions, which is reflected in the sliding calculations. In Fig.5a, the solutions to Eq.8 are displayed. For all  $l/h > 0$ , the maximum displacement is inferior to the case without a plate. However, the reduction of the sliding is insignificant, with a maximum of 2.1%. Comparing these with the sliding due to only the horizontal force<sup>2)</sup> in Fig.5b, it is evident the importance of considering the vertical force to represent the hydrodynamic phenomena more accurately.

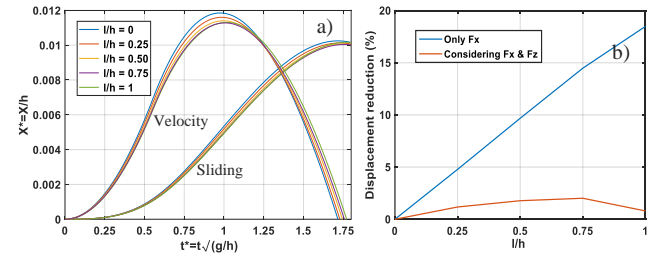


Fig. 5 a) Dimensionless displacement/velocity  
b) Displacement reduction. Comparison without and with  $F_z$ .

## 4. Conclusions and recommendations

The following findings were obtained from this study:

- 1- The Boundary-Point Selection Method (BPSM) is applicable with excellent results in finding solutions for boundary problems related to breakwaters with horizontal plates (as long as the division regions are rectangular).
- 2- The inclusion of the vertical force in the sliding analysis of caisson with horizontal plates gives more accurate results. Not including it leads to overestimating the horizontal plate's positive influence in reducing the sliding, especially for large  $l/h$  ratios.
- 3- Horizontal plates have a minimal influence on the overall sliding of breakwaters' caissons. (Sliding reduction  $\leq 2\%$ )
- 4- For the new shapes of caissons' design seeking to reduce sliding due to increments on the added mass because of water constriction, the new elements should induce an increment on the horizontal added mass but a reduced or no vertical added mass.

## References

- 1) Aoki, S. and Okube, A. Proceedings of Coastal Engineering, Vol.42, pp.861-865, 1995. (in Japanese)
- 2) Yoshihara, M. Master thesis. Civil Engineering Department, Osaka University, 2019. (in Japanese)
- 3) Yoshida, A, Kojima, H and Tsurumoto, Y. JSCE Proceedings, No.42/II-13, pp.265-274, 1990. (in Japanese)

# Capsizing & Survivability of Ships Based on Safe Basin's Fractals

Colin Fatuimoana Langilangi

Ship Intelligentization Subarea, Naval Architecture and Ocean Engineering

**Key Words:** Safe basin, Flip bifurcation, Ship capsize, Chaos, Periodic solutions

## 1. Introduction

On August 5th 2009, the ferry MV Princess Ashika capsized and sank approximately 75 miles Northeast off the coast of the capital Nuku'alofa, of Tonga. The tragedy claimed 74 lives mostly women and children, thus highlighting the fact that capsizing is one of the most threatening events that a vessel could encounter at sea. As evident from the consequence of the 2009 disaster, capsizing leads to critical death tolls. Consequently, it is a vigorous commission to obtain resolutions to avert the capsizing of ships at sea, guaranteeing the safety and security of maritime transportation.

The term referred to as capsizing can be described as when a ship encounters itself in a situation when it is turned on its side or is upside down in the water. A reasonable quantity of researches has been carried out determining that the frequent reasons for the capsizing of ships are due to determinants such as parametric roll resonance, broaching-to, water on deck, or the loss of stability at a wave crest.

In courses of nonlinear dynamics, it is further recognised as a shift from a stable equilibrium point near the upright position into a stable equilibrium point near the upside-down position. Yet, stemming from the 1980s advancements into nonlinear dynamics, a significant number of enhanced computational capabilities unlocked new possibilities in the investigation of such a complex phenomenon. One of those studies is of what is known as the safe basins, which was employed in an attempt to surmise the mechanics behind capsizing.

In the study, the author focuses on the exact and approximation of boundaries of safe motion in the space of control parameters. Based on the published investigation of vessel capsizing utilising this method conducted by Kan and Taguchi <sup>1)</sup> and others <sup>2)</sup>, the author implements the application of the method on a real-life ship in regular waves. The container ship of the ITTC Ship A1 has been the subject ship of choice employed in this study. Due to the restoring term having a cubic polynomial in naval engineering, along with a simplified form of the GZ plotted curve of the ship, the author proceeds with setting towards a 9th order polynomial.

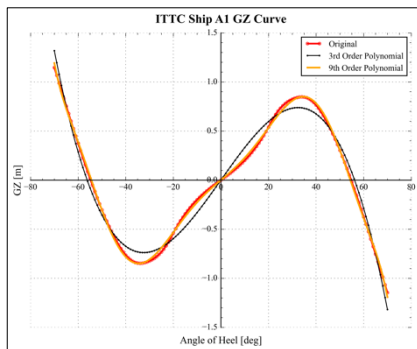


Fig.1 ITTC Ship A1 GZ Curve

In past readings, manageable equations have been utilised to

model the vessel's equation of motion, where it is capable to represent the roll motion using Newton's second law and contain a quadratic or cubic polynomial term in the restoring moment. Damping was then considered to be linear, while regular waves were considered as external interference.

In this paper the following equation has been used to model the ITTC Ship A1 in quartering regular waves:

$$\ddot{\phi} + \beta_1 \dot{\phi} + \beta_2 |\dot{\phi}| + \beta_3 \dot{\phi}^3 + \alpha_1 \phi + \alpha_3 \phi^3 + \alpha_5 \phi^5 + \alpha_7 \phi^7 + \alpha_9 \phi^9 = B \cos(\omega t) \quad (1)$$

where  $\beta_1, \beta_2, \beta_3, \omega$  and  $B$  are constants representing the normalized damping coefficient, the non-dimensional frequency and amplitude of the exciting moment, respectively,  $\alpha_1, \alpha_3, \alpha_5, \alpha_7, \alpha_9$  represents the restoring term through 9<sup>th</sup> order polynomial, and  $\phi$  is the normalized angle of roll and  $t$  is the normalized time. The dots signify the differentiation with respect to the normalized time. The equation (1) has produced a range of distinctive behaviors, including steady-state solutions and flip bifurcation that eventually leads to chaos. The following sections are descriptions of the safe basins, its concept and how it has been applied for the case of the capsizing equation (1).

## 2. Safe Basin & Application

### 2.1 Safe Basin Concept

The safe basin primarily are sets of initial conditions within a phase plane  $(\phi, \dot{\phi})$  which define the variance between capsizing and non-capsizing regions and demonstrates the sensitivity of capsizing to the initial conditions. With the insertion of parameters  $(\beta, \alpha, B, \omega)$ , the safe basin of attraction is formed by all initial conditions of  $(\phi(0), \dot{\phi}(0))$  that does not capsize.

### 2.2 Safe Basin Application

The safe basin in the paper is generated numerically by course grid-of-start method. The calculations are then run by the increasing of the amplitude of excitation, which leads to a process of fractal erosion within the safe basin.

The capsizing equation (1) is then solved numerically and lopped through various initial conditions of  $B$  using the Runge-Kutta method, implementing through Python. The system is then run for 100 cycles of forcing (period  $T = 2\pi/\omega$ ). The initial conditions  $(\phi(0), \dot{\phi}(0))$  were then tried against a vast set of  $641,601 = 801 \times 801$  points, and are obtained by also dividing the plane  $[-1.222, 1.222] \times [-1.5, 1.5]$  into equally spaced divisions. The points are then calculated against the criterion (vanishing angle), and sorted if capsizing occurs or not. When the calculation return is safe, the program places a small black dot in the phase plane  $(\phi, \dot{\phi})$ . If the return is not safe, then the plane maintains white. Therefore, the safe basin is defined by the black area that is presented by the phase plane. The fractal erosion observed by the

safe basin in this paper follows a different shape and route compared to those from the previous studies, which are owed up to the increasing of the excitation amplitude  $B$  and the introduction for a 9<sup>th</sup> order polynomial to the governing equation (1).

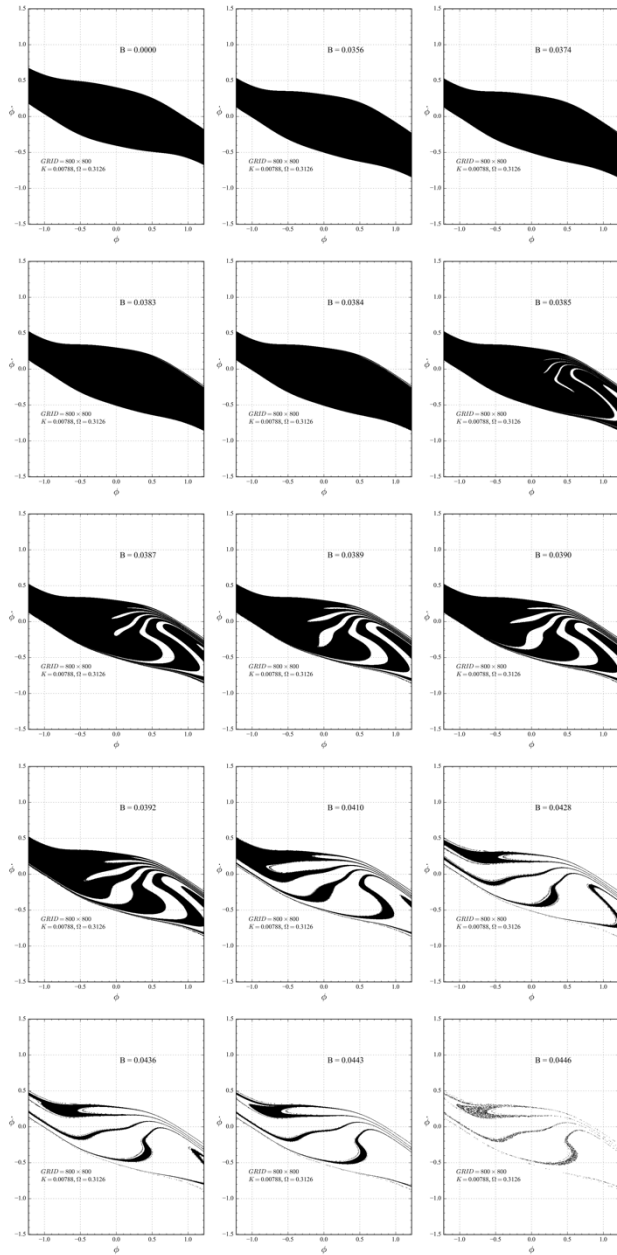


Fig.2 ITTC Ship A1 Safe Basin & erosion observed

### 3. Poincare Bifurcation Diagrams & Map

#### 3.1 Bifurcation Diagrams

Now that the safe basin has been illustrated, further study was then carried out on the final safe state points of the system with each given condition. In this case, the colors of the plots are altered in order to easily distinguish the behavior of the points and when bifurcation occurs. As observed, the system begins with a single point of final safe state as expected when  $B = 0.0$ . Overtime interesting cases arise with the observations of two points returned, thus showing evidence of bifurcation at that point in time. However,

there are also cases of multiple points being observed, perhaps to be signs of chaotic behavior present within those specific regions of the safe basin.

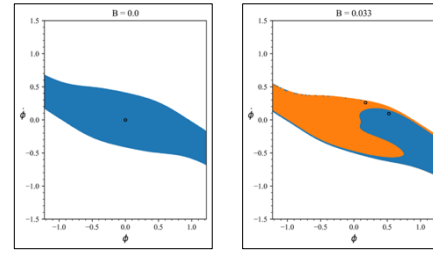


Fig.3 Bifurcation Diagram of the safe basin of  $B = 0.0, B = 0.033$

#### 3.2 Poincaré Bifurcation Diagram

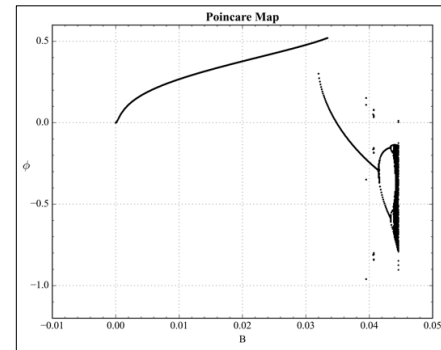


Fig.4 Poincaré Map Diagram showing behavior of points of various  $B$  values.

The assembly of the Poincaré map further supported the behavior of the points return in the bifurcation diagram plots, showing a more comprehensible visual of the events occurring.

### 4. Conclusion

In this study, the meticulous numerical analysis of the safe basin's fractal erosion was conducted on the ITTC A1 container ship, adopting a revised symmetric capsizing equation to the equation utilized by Kan and Taguchi <sup>1)</sup> and <sup>2)</sup>. Distinct erosions of the safe basin were presented with bifurcation occurring. The paper recognizes the correspondence of data that the safe basin and GZ curves offer in setting measures that ships could operate within, ensuring the safety and security of maritime transportation when averting the case of capsizing.

### References

- 1) Maki, A., Virgin, L., Umeda, N., Ueta, T., Miino, Y., Sakai, M., & Kawakami, H. (2019). On the loss of stability of periodic oscillations and its relevance to ship capsizing. *Journal of Marine Science and Technology*, 846-854.
- 2) Kan, M., & Taguchi, H. (1990). *Capsizing of Ships in Quatering Seas (Part 2. Chaos and Fractal in Capsizing Phenomenon)*.

# Development of Automatic Evaluation System of Underwater Vehicle's Motion Performance Based on OpenFOAM

LI JUNJIAN

Marine hydro-science and engineering lab,  
Naval Architecture & Ocean Engineering

**Key Words:** Underwater Vehicles, CFD, Python, openFOAM, Hydrodynamic Coefficients, Automatic Control System

## 1. Introduction

Nowadays, Computational Fluid Dynamic method (CFD) have become wildly used in the design of ships and underwater vehicles. However, the operation of CFD requires a lot of hydrodynamic learning and experience. And it is difficult for beginners to evaluate the performance of ships or underwater vehicles using CFD methods. Under these circumstances, open source codes of CFD method are highly recommended to use. Since most of open source codes of CFD method are free and they are often used in the evaluation of the maneuverability of underwater vehicles with relatively small size, the development of automatic evaluation system of underwater vehicle's motion performance is of great significance.

Nevertheless, as mentioned above, to use CFD method and derive convincing results, researchers need to accumulate a certain amount of CFD knowledge and experience. Therefore, in this research, our laboratory aimed to develop a CFD-based performance estimation tool for underwater vehicles which can obtain the results with reasonable accuracy if only the CAD data of body shape of vehicles are given. Even relatively small underwater vehicles' manufacturers can use this estimation tool for basic motion performance simulations.

## 2. Previous research

Automatic Change and Correction System (ACCS) was developed by Mr. Takada who was a member of the lab. The way of distinguishing between Work Type AUV and Cruise Type AUV from triangle quality of CAD data has been founded. And three degrees of freedom, which compose basic motion of underwater vehicles, is adopted. Analyzing the results from three tests with multiple regression analysis, Hydrodynamic Coefficients can be obtained. The equations of Fluid forces acting on the underwater vehicles and three tests for hydrodynamic performance are shown in Fig. 1.

| Fluid force acting on the underwater vehicle  |
|---|
| There are <b>6 degrees of freedom</b> of underwater vehicles. In ACCS, the <b>3 degrees</b> which compose basic motion of underwater vehicles is adopted.   |
| $\begin{aligned} X_H'(v_m, r') &= X_0' + X_{\dot{v}_m} v_m'^2 + (X_{\dot{v}_m} + m' + m'_y) v_m' r' + (X_{\dot{v}_m} + x'_G m') r'^2 + X_{\dot{v}_m} v_m'^4 \\ Y_H'(v_m, r') &= Y_0' + Y_{\dot{v}_m} v_m' + (Y_{\dot{v}_m} - m' - m'_x) r' + Y_{\dot{v}_m} v_m'^2 r' + Y_{\dot{v}_m} v_m' r'^2 + Y_{\dot{v}_m} r'^3 \\ N_H'(v_m, r') &= N_0' + N_{\dot{v}_m} v_m' + (N_{\dot{v}_m} - x'_G m') r' + N_{\dot{v}_m} v_m'^2 + N_{\dot{v}_m} v_m' r' + N_{\dot{v}_m} v_m' r'^2 + N_{\dot{v}_m} r'^3 \end{aligned}$ |
| $X_H'$ :longitudinal force $Y_H'$ :lateral force $N_H'$ :turning moment $r'$ :turning angular velocity $v_m'$ :lateral velocity   |
| The 3 tests which is needed for hydrodynamic performance  |
| <ol style="list-style-type: none"> <li>1. CAT (Constant Acceleration Test)</li> <li>2. CMT (Circular Motion Test)</li> <li>3. OTT (Oblique Towing Test)</li> </ol>  |

Fig. 1 The calculations in ACCS

## 3. Hydrodynamic coefficients

Here, the added mass coefficient is described as an example of the hydrodynamic coefficient. Added mass is the pressure

induced forces and moments due to fluid accelerating with an accelerating body. When a body is accelerating in any direction, it has to accelerate the surrounding fluid as it is moving through it which requires additional forces and moments than if the vehicle was moving in vacuum. It is important to note that there is no distinct mass of fluid moving with a specific acceleration; it is just a convenient way of describing the additional forces and moments. In reality, all fluid particles surrounding the submerged body will move with different acceleration. The hydrodynamic forces caused by added mass can be derived as follow:

$$\begin{Bmatrix} X_{am} \\ Y_{am} \\ Z_{am} \\ K_{am} \\ M_{am} \\ N_{am} \end{Bmatrix} = -M_a \frac{d}{dt} \begin{Bmatrix} u \\ v \\ w \\ p \\ q \\ r \end{Bmatrix} \quad (1)$$

Where  $M_a$  is the added mass matrix with a six degree of freedom system, which also called 6DOF. The linear motions surge, sway and heave and the angular motions roll, pitch and yaw are included in the six degree of freedom system, which are presented in Table 1. And the notation used for these motions are according to SNAME (1950).

Table 1 Notation according to SNAME

| Degree of Freedom | Motion                         | Forces and moments | Linear and angular velocities |
|-------------------|--------------------------------|--------------------|-------------------------------|
| 1                 | Surge (Motion in x-direction)  | $X$                | $u$                           |
| 2                 | Sway (Motion in y-direction)   | $Y$                | $v$                           |
| 3                 | Heave (Motion in z-direction)  | $Z$                | $w$                           |
| 4                 | Roll (Rotation around x-axis)  | $K$                | $p$                           |
| 5                 | Pitch (Rotation around y-axis) | $M$                | $q$                           |
| 6                 | Yaw (Rotation around z-axis)   | $N$                | $r$                           |

After the expansion of added mass matrix, the hydrodynamic forces can be defined as follow:

$$M_a = \begin{bmatrix} m_{11} & m_{12} & m_{13} & m_{14} & m_{15} & m_{16} \\ m_{21} & m_{22} & m_{23} & m_{24} & m_{25} & m_{26} \\ m_{31} & m_{32} & m_{33} & m_{34} & m_{35} & m_{36} \\ m_{41} & m_{42} & m_{43} & m_{44} & m_{45} & m_{46} \\ m_{51} & m_{52} & m_{53} & m_{54} & m_{55} & m_{56} \\ m_{61} & m_{62} & m_{63} & m_{64} & m_{65} & m_{66} \end{bmatrix} \quad (2)$$

Even with ACCS, many of these added mass components and other hydrodynamic force coefficients cannot be calculated, and in order to calculate them, it is necessary to perform simulations such as forced oscillation. Therefore, in the new system, I decided to aim at further automation of mesh generation and automatic execution of forced oscillation test by CFD.

## 4. CFD method



#### 4.1 Previous method

In order to estimate the motion performance of underwater vehicles, four basic steps are needed, importing, meshing, calculating and analyzing. Using previous method, settings of initial values, meshing and calculation solver should be changed manually according to different imported geometry, which takes plenty blank time.

#### 4.2 Proposed method

Automatic Grid Study System (AGSS) has been developed in this research, which can conduct the studies of side walls and grid independence. Referring to geometry information obtained from CAD data, turbulence parameters, such as Turbulence kinetic energy  $k$  and turbulence dissipation rate  $\varepsilon$ , can be calculated automatically. Meanwhile, simulation results using different meshing strategies can be obtained by this automatic estimation system. After importing the CAD data of objective geometry, this system can execute the calculations for each case continually, which can save a lot of time.

### 5. Flow of proposed method

#### 5.1 AGSS 1<sup>st</sup> step (Importing)

AGSS system inputs CAD file and processes CAD information and outputs the processed CAD information, for example, length, breadth, depth, center of masses and structure complexity. As the previous research, it can also distinguish the cruise type or work type of underwater vehicles by triangle quality. According to the type of underwater vehicles, different strategies of simulations will be adopted. And relative size or absolute size of boundary layers will be added close to the geometry.

#### 5.2 AGSS 2<sup>nd</sup> step (Pre-Calculation)

The hydrodynamic parameters will be automatically calculated, such as Reynolds number, turbulence kinetic energy and turbulence dissipation rate, etc. Then first layer thickness will be calculated by these 4 steps, skin friction, wall shear stress, friction velocity and wall distance. The settings for initial values and boundary layers will be replaced by the calculated values.

#### 5.3 AGSS 3<sup>rd</sup> step (Grid Study)

From the last step, the cad information after processing was derived. Fig. 1 shows the calculation domain. Different mesh strategies will be created respectively. Using refinement ratio, 5 meshes of different minimum size will be used.

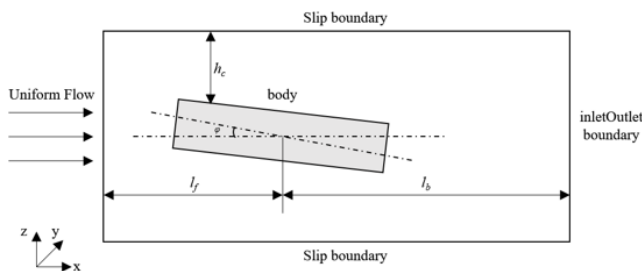


Fig. 1 Calculation domain and boundary conditions

#### 5.4 AGSS 4<sup>th</sup> step (Results Analysis)

After the calculations are finished, the forces and force

coefficients data can be obtained by two post-processing commands. For visual analysis, 'paraFoam' will be used to check pressure and velocity distribution.

#### 5.5 AGSS 5<sup>th</sup> step (Motion Test)

Then the proper mesh strategy will be picked up for motion test. Constant acceleration test was conducted in the previous research. Assuming the speed resistance is negligible, the fluid force is calculated immediately after 0.001 second, the object starts accelerating. For motion oscillation test, dynamic mesh will be used. Force oscillation test can also be conducted in this step. The imported geometry will move with the oscillation in x-z plane. Dynamic mesh and transient solver will be used. Calculated drag coefficients with time history will be outputted. The map of this system is shown in Fig. 2.

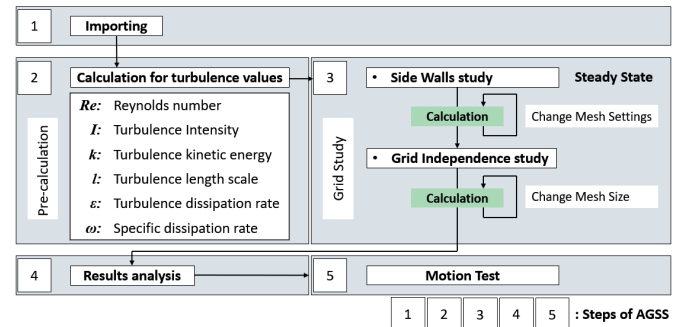


Fig. 2 The map of proposed method

### 6. Conclusion

- Comparing with the previous estimation system ACCS, new automatic estimation tool, which can conduct Side Walls Study, Grid Independence Study and Force Oscillation Test, has been developed.
- Different from ACCS system, and to get the results with a certain accuracy, parameters of turbulence model can be calculated according to the imported geometry. And the settings of initial values will be changed automatically.
- Because of wall function used in  $k-\omega$  SST model, AGSS system can use y plus to calculate the first layer thickness and add boundary layers with absolute size automatically.

### References

- Suzuki, H.; Sakaguchi, J.; Inoue, T.; Watanabe, Y.; Yoshida, H. Evaluation of methods to estimate hydrodynamic force coefficients of underwater vehicle based on CFD. IFAC Proc. Vol. 2013, 46, 197-202.
- SNAME. 1950. Nomenclature for treating the motion of a submerged body through a fluid. Tech. rept. Technical and Research Bulletin 1-5, Hydrodynamics Subcommittee of the Technical and Research Committee, Society of Naval Architecture and Marine Engineers.
- Takada Yukihiro: "Development of Automatic Calculation System for Hydrodynamics Analysis of AUV by using Python Programs", Osaka University (2020).
- Josefine Severholt: "Generic 6-DOF Added Mass Formulation for Arbitrary Underwater Vehicles based on Existing Semi-Empirical Methods", Royal Institute of Technology, 2017.

# Microcomputer Control of Underwater Vehicle with Undulating Side Fins

Lin ShenChi

Sub-area of Marine Hydro-Science and Engineering, Department of Naval Architecture and Ocean Engineering

**Key Words:** *Squid-like underwater robot, Course keeping, Zig Zag test, Williamson Turn, Data analysis*

## 1. Introduction

The propulsion system of squid-like body with undulating side fins have been investigated in our laboratory for several years. This propulsion system is designed the operation at a moderate speed and can easily perform six degrees of freedom motion by adjusting direction and phase velocity of the side fins. It produces propulsive force and control force for such as direction change by moving the side fins in a traveling wave shape and create with little vertical movement and easy for seabed exploration.

The purpose of this study is to reduce the volume and control system of model-7 correspond to model-5 by using smaller spaces and microcomputers to control the motor rotation for the fins and to control the course keeping of the model. Also, with 360-degree camera for complicated structure underwater exploring and returning the images and videos.

## 2. Experiment Overview

### 2.1 Overview of model-7

The traveling wave motion of side fins are produced by scotch-yokes and covered by rubber to increase its fluidity. A tail fin is designed behind the body to control the depth. Motors, batteries, drivers and control system including various micro computers are installed inside the watertight polyvinyl chloride (PVC) body. The vehicle model particulars are as shown in Table 1 and Fig.1 shows the body of model-7.

Table. 1 Principal particular

|                         |           |
|-------------------------|-----------|
| Length                  | 57.0cm    |
| Width                   | 22.8cm    |
| Height                  | 6.0cm     |
| Weight                  | 4.5kg     |
| Fin Length              | 7.0cm     |
| Number of fins          | 7(tot 14) |
| Length between each fin | 5.0cm     |



Fig. 1 Model-7

### 2.2 Manual Control

Control systems using gyro sensor for course keeping, zig zag test and Williamson turn in bigger model were conducted last year. For present study, the smaller system is designed by using two Teensy 4.1 instead of stick PC and Arduino MEGA. But the final installation could not be done due to time limitation, Manual control using microcomputers were tested in towing tank. Microcomputer, transmitter and receiver used for manual control are shown in Fig.2 and Fig.3.

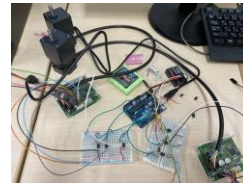


Fig. 2 Microcomputers



Fig. 3 Transmitter and Receiver

In this study, two brushless motors were used for manual control. The transmitter for proportional control as shown in Fig.3 controlled the slope of right- and left-hand control sticks to make the forward and backward rotation of the left and right motors. By the microcomputer, the signal for changing the rotation direction by making short- circuited accordingly, and voltage for number of revolutions was applied to the drivers to control the rotation speed. By combining right and left sticks' movement, the model could move free and stable. The example of manual control is shown in Fig.4. It shows the turning motion.



Fig. 4 Manual Control Running

### 2.3 360-degree camera

For the one of the sensors, 360-degree camera (Ricoh Theta sc2) shown in Fig.5 was used in the free-running tests. The camera can be used to discover the situation of underwater. Due to the manipulate, such as course keeping, rotation and changing depth by tail fin, clear surroundings could be found after sending back the videos and images as shown in Fig.6. It can be connected by Wi-Fi connection to the smart phone and can be controlled and store the video images. To make the Wi-Fi connection available in the water, the pipe should be installed from camera watertight case to the float. In this study, the control

was done when the vehicle was floating.



Fig. 5 camera



Fig. 6 surroundings underwater

## 2.4 Preliminary experiment of Gyro Sensor

The gyro sensor (BNO055) shown in Fig.7 would be used in model-7 for processing the data of yaw angle and yaw rate. For the sensor, the switch signal by the transmitter could be sent to reset the yaw angle to 0 degree. The test using gyro system (BNO055 and Arduino Nano) was tested in laboratory for preliminary test. The test time history is shown in Fig.8.

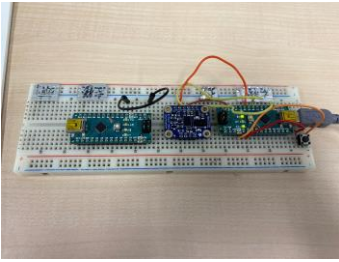


Fig. 7 Gyro Sensor

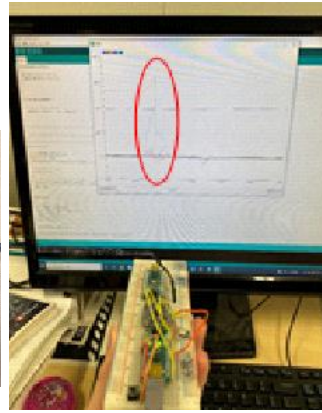


Fig. 8 Preliminary test of Gyro

## 3. Simulation

The gyro sensor data could be sent back to the main Arduino for course keeping, zig zag test, Williamson turn maneuvers. Some control strategies were simulated by 6DOF simulation program by using equations of motion and hydrodynamic force model. Here 3DOF results were shown.

### 3.1 Course keeping maneuver

The course keeping maneuver simulation was done using PD control. The equation for PD control is shown below.

$$\Delta f = -K_p(\psi - \psi_t) - K_d\dot{\psi}$$

$\Delta f$ : Frequency difference between left and right fins

$K_p$ : Proportional gain  $K_d$ : Differential gain

$\psi$ : Yaw angle  $\psi_t$ : Target yaw angle  $\dot{\psi}$ : Yaw rate

When  $K_d = 0$ , it becomes the equation for P control.

The computation was done for various initial angle and speed. But the results are not shown here, because the course keeping maneuver was used in the last stage of Williamson Turn.

### 3.2 Zig Zag Test

In the simulation of zig zag maneuver with transition absolute

yaw angle of  $30^\circ$ ,  $60^\circ$ ,  $90^\circ$  and  $\Delta f = 0.3$  were executed.

( $f_R = 1 f_L = 0.7$  or  $f_L = 1 f_R = 0.7$ ) The zig zag motions with three different transition angles are shown in Fig.9. The yaw angle time histories for  $30^\circ$  is shown in Fig.10.  $\psi$  is known as yaw and  $\Delta f$  is known as the command value in the figure.

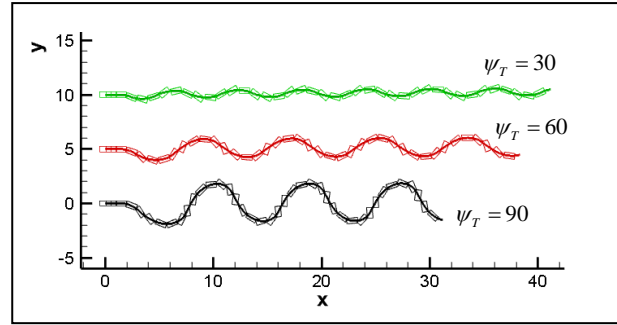


Fig. 9 Three Different Angles

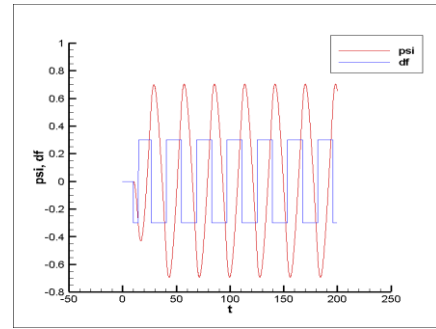


Fig. 10 Simulation of  $30^\circ$

### 3.3 Williamson Turn

The Williamson turn is a maneuver used to bring a vehicle under power back to a point it previously passed through. In this model, after course keeping with the target angle of  $0^\circ$  for a while, it turned right to the target  $\Theta_1$ , and started turning left when it reached  $\Theta_2$  and kept course keeping at the target angle  $-180^\circ$ . The proper trajectory angle of Williamson Turn in this model is  $60^\circ$  for  $\Theta_1$  and  $165^\circ$  for  $\Theta_2$  as shown in Fig.10. The relation between turning circle and  $\Delta f$  is shown in Fig.11.

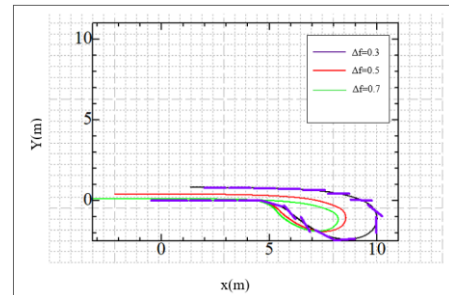


Fig. 10 Williamson Turn in Three Different Frequencies

## 4. Conclusions

The manual control using microcomputers, transmitter and receiver for model-7 could be performed and the model could be controlled easily. Smaller model could be controlled easier than the big one. With a 360-degree camera, discovering even a complicated structure underwater could be achieved. In addition, gyro sensor simulations on this model were tested this year.